Pacific Northwest
NATIONAL LABORATORY

PNNL-36803

Development of Operando Atom Probe to study field-assisted surface chemistry

September 2024

Sten V Lambeets
Mark G Wirth
Eric Vo
Shawn Kathmann
Daniel E Perea

U.S. DEPARTMENT OF ENERGY

Prepared for the U.S. Department of Energy
under Contract DE-AC05-76RL01830

DISCLAIMER

This report was prepared as an account of work sponsored by an agency of the United States Government. Neither the United States Government nor any agency thereof, nor Battelle Memorial Institute, nor any of their employees, makes **any warranty, express or implied, or assumes any legal liability or responsibility for the accuracy, completeness, or usefulness of any information, apparatus, product, or process disclosed, or represents that its use would not infringe privately owned rights**. Reference herein to any specific commercial product, process, or service by trade name, trademark, manufacturer, or otherwise does not necessarily constitute or imply its endorsement, recommendation, or favoring by the United States Government or any agency thereof, or Battelle Memorial Institute. The views and opinions of authors expressed herein do not necessarily state or reflect those of the United States Government or any agency thereof.

PACIFIC NORTHWEST NATIONAL LABORATORY
operated by
BATTELLE
for the
UNITED STATES DEPARTMENT OF ENERGY
under Contract DE-AC05-76RL01830

Printed in the United States of America

Available to DOE and DOE contractors from
the Office of Scientific and Technical Information,
P.O. Box 62, Oak Ridge, TN 37831-0062
www.osti.gov
ph: (865) 576-8401
fox: (865) 576-5728
email: reports@osti.gov

Available to the public from the National Technical Information Service
5301 Shawnee Rd., Alexandria, VA 22312
ph: (800) 553-NTIS (6847)
or (703) 605-6000
email: info@ntis.gov
Online ordering: http://www.ntis.gov

PNNL-36803

Development of Operando Atom Probe to study field-assisted surface chemistry

September 2024

Sten V Lambeets
Mark G Wirth
Eric Vo
Shawn Kathmann
Daniel E Perea

Prepared for
the U.S. Department of Energy
under Contract DE-AC05-76RL01830

Pacific Northwest National Laboratory
Richland, Washington 99354

Abstract

Recent efforts at PNNL have led to the development of in-situ Atom Probe Tomography (ISAPT) and Operando Atom Probe (OAP), establishing PNNL as a key player in this technology, both in the U.S. and globally. OAP has already pushed the initial limits of APT, which was traditionally used at cryo temperatures (<60 K) and ultra-high vacuum (<10^{-12} bar), to operate in the presence of reactive gases (up to 10^{-10} bar) at a maximum temperature of 300 K. Using OAP, we successfully observed Co and Fe oxidation in real-time at the nanoscale, revealing the importance of surface structures in these interactions. Additionally, OAP opens the possibility to explore the influence of local electric fields (EFs) on surface chemistry and hydrogen interactions at the nanoscale.

In this work, we expanded the capabilities of OAP to observe Fe oxidation and N_2 dissociation on Ru under high electric fields in real-time, in the simultaneous presence of hydrogen. OAP observations, combined with Field Ion Microscopy (FIM) characterization, revealed that Fe oxidation primarily occurs on open facets such as Fe{244} and Fe{112}, while high-coordination facets like Fe{024}, Fe{013}, and Fe{011} remain relatively resistant to oxidation. Supported by DFT calculations and a mean-field model developed by Prof. Jean-Sabin McEwen's group (WSU), our results demonstrate that intense EFs polarize and attract gas molecules toward the surface, effectively increasing local pressure through electric field enhancement at the tip's apex. However, excessive EFs mitigate Fe oxidation due to field evaporation and reduced oxygen binding strength, as shown by our DFT-based model. These findings suggest that EFs could dynamically influence chemical reactions across a broad range of systems.

We extended this methodology to detect the dissociative adsorption of N_2 and H_2 at room temperature. Ru(0001), {10-12}, and {11-24} facets played key roles in these dissociations. Although accurately estimating the surface electric field values remains challenging, FIM surface characterization, enhanced by quantum mechanics calculations, allowed us to narrow the field intensity of interest to between 13 and 15 V/nm. Ongoing collaborations with Shawn Kathmann are in progress to refine our understanding of these systems, positioning OAP as a valuable tool for studying field-assisted chemistry and expanding research opportunities.

We also encountered challenges during the development of a new atom probe, particularly with the integration of a Raman detector, due to the fragility and size of the APT specimen. Despite these setbacks, we improved electric field estimations through detailed FIM image analysis and developed methods using Kingham plots and APT mass spectra at different temperatures.

The OAP setup was successfully adapted for hydrogen-related investigations, with further advancements made in data analysis and high-temperature capabilities. Future work will focus on applying extreme electric fields to C(diamond) specimens in collaboration with Prof. Peter Pauzauskie, aiming to observe N_2 dissociation on C(diamond).

Summary

Recent efforts at PNNL have led to the development of in-situ Atom Probe Tomography (ISAPT) and Operando Atom Probe (OAP), establishing PNNL as a key player in this technology, both in the U.S. and globally.

This work reports our recent efforts to extend OAP capabilities to study hydrogen surface interactions, focusing on two specific cases: H_2 + O_2 on Fe and N_2 + H_2 on Ru. Combined with Field Ion Microscopy (FIM) characterization, OAP allows us to detect which crystal structures are more sensitive to the presence of these reactive gases in real-time.

Our findings show that Fe{112}, {244}, and {222} are the most sensitive regions to O_2, while Fe{011}, {024}, and {013} are the most sensitive to H_2. Our experimental observations were successfully compared with DFT models, revealing the "double-edged" effect of the electric field. While the electric field increases the rate of dissociative adsorption of O_2, it also alters the thermodynamic equilibrium of the system, reducing the maximum O coverage on the surface.

OAP successfully demonstrated the possibility of dissociating N_2 at room temperature with the assistance of electric fields. The challenge was to narrow down the electric field intensity at which this phenomenon occurs. We developed new methods based on Kingham plots, which report the relative abundance of charged ions over the intensity of the electric field, to perform our estimations. We found that N_2 dissociation on Ru is possible with electric fields as intense as 13-15 V/nm. Ru{0001}, {10-12}, and {11-24} seem to play key roles in this dissociation. When simultaneously exposed to H_2, H_2 and N_2 appear to compete for the same regions to achieve their dissociative adsorption.

Finally, this report also addresses technical developments beyond the installation of hydrogen feeds. We have improved our data processing software and developed a new high-temperature puck, which is still in the testing phase.

Acknowledgments

This research was supported by the Open Call Initiative, under the Laboratory Directed Research and Development (LDRD) Program at Pacific Northwest National Laboratory (PNNL). PNNL is a multi-program national laboratory operated for the U.S. Department of Energy (DOE) by Battelle Memorial Institute under Contract No. DE-AC05-76RL01830.

Acronyms and Abbreviations

APT	Atom Probe Tomography
DFT	Density Functional Theory
EF	Electric Fields
EEF	External Electric Field
FIM	Field Ion Microscopy
LEAP	Local Electrode Atom Probe
OAP	Operando Atom Probe
ToF-MS	Time-of-Flight Mass Spectrometry

Contents

Abstract ii
Summary iii
Acknowledgments iv
Acronyms and Abbreviations v
1.0 Introduction 1
2.0 Elucidating the Role of Electric Fields in Fe Oxidation via Environmental Atom Probe 2
2.1 Specimen preparation and FIM characterization 2
2.1.1 Fe specimen preparation 2
2.1.2 Field Ion Microscopy 3
2.1.3 Atom Probe Tomography, field evaporation cleaning and electric field estimation 3
2.1.4 Field-assisted Fe oxidation Model 4
2.1.5 Differential adsorption of $^{2}H_2$ and $^{18}O_2$ on Fe in presence of electric field 6
2.1.6 Normalized Oxygen Distribution on the Fe Surface 8
2.2 Conclusion and perspectives 9
3.0 Tracking N_2 field-assisted dissociation on Ruthenium and Iron by Operando Atom Probe 10
3.1 Methods 12
3.1.1 Field Ion Microscopy characterization of Ruthenium 12
3.2 N_2 field-assisted dissociation on Ru 14
3.2.1 N_2 field dissociation 14
3.2.2 Differential adsorption of N_2 and $^{2}H_2$ on Ru 16
3.3 Surface electric field and impact on N_2 Molecular orbitals 17
3.4 Conclusions and perspectives 18
4.0 Technical developments of OAP 19
4.1 OAP results analytic software. 19
4.2 High temperature specimen holder 19
5.0 References 21
Appendix A – List of APT experiment with ID # runs A.1

Figures

Figure 1: The electronic and chemical properties of a surface are defined by the surface's near-electric field, presenting opportunities to continuously modulate surface chemical properties with an external electric field (EEF). This field-assisted surface chemistry approach uses EEFs to deform N2 molecular orbitals and enable their dissociation at room temperature on inexpensive and abundant metals. 1

Figure 2.1 (A) FIM image (left) and associated ball model (right) of a (011)-oriented Fe needle specimen. Conditions of acquisition: 45.0 K, 3300 V (~35 V/nm), P(Ne) = 2.2×10^{-6} mbar. Main facets identified are Fe{112}, Fe{013}, Fe{244} and a central Fe(011). 3

Figure 2.3: (A) Calculated E_{ads} of oxygen atoms on iron at the different coverages for the four facets. The electric field was varied from -10.0 V/nm to +20.0 V/nm in increments of 2.5 V/nm. (B) Changes in Eads by application of a positive 10.0 V/nm (solid bar) or negative 10.0 V/nm (checkered bar) electric field. Changes are in reference to no electric field applied. All coverages tested. 4

Figure 2.4: Experimentally measured 2D projection composition maps of (A) O(%)atomic, (B) Fe_2O^{n+}ionic of a Fe specimen exposed to 1.2×10^{-7} mbar of pure O_2 with a constant 15 V/nm (24.8 V/nm pulsed) applied EF at room temperature. The experimental composition maps shown are displaying the average composition detected over a 5 min time lapse (C) Theoretically derived 2D projection composition maps from corresponding first principles-based model of evolving oxygen coverage over a field emitter tip with an EF of 24.12 V/nm, a pressure of 1.1×10^{-8} mbar and a temperature of 300 K. 6

Figure 2.7: Mass spectra of a Fe specimen exposed to ~$1x10^{-8}$ mbar of $^{2}H_2$+$^{18}O_2$ (1:1) gas mixture at 300 K while applying ~15 V/nm on the surface. 7

Figure 2.8: FIM characterization of Fe specimen, and its surface composition found by OAP while exposed to ~$1x10^{-8}$ mbar of $^{2}H_2$+$^{18}O_2$ (1:1) gas mixture at 300 K while applying ~15 V/nm on the surface..... 7

Figure 2.11: Snapshots of the time evolution of oxygen coverage on the Fe crystallite at 1.1×10^{-8} mbar and 700 K under (A) 25 V/nm and (B) 30.5 V/nm applied electric fields. (C) Time evolution of oxygen coverage under varying electric fields with the inset highlighting the first 60 seconds. (D) Snapshots of the time evolution of oxygen coverage on the multifaceted crystallite for the first 10 seconds in the presence of an electric field of 30.5 V/nm. 8

Figure 3.1: Electronic bonding (green) and anti-bonding (burgundy) orbitals for N2 (N blue) and CO (C gray, O red) in zero field and in 62 V/nm[25]..... 11

Figure 3.2: Schematic description of the sharpening process. (a) N2 can only adsorb to the tip shank where the field is lower than at the apex. (b) The W-N bond weakens the bonding of the W atoms to the tip, and they field evaporate, leading to a preferential loss of material around the tip shank. (c) Tip profile before etching (blue), and after (red), illustrating a reduction in

local radius of curvature at the apex and the final “shouldered” shape of the tip[5].....12

Figure 3.3 (left) Mass spectra of Ru specimen Field evaporation cleaning by APT. (right) Kingham plot of Ru reporting the relative abundance of Ru^{+}. Ru^{2+} and Ru^{3+} depending of the intensity fo the electric field triggering the field evaporation. 13

Figure 3.4: (left) FIM image of a (0001)-oriented Ru needle specimen. Conditions of acquisition: 45.0 K, 5500 V (~35 V/nm), Main facets identified are Ru(0001), Ru{1124} and Ru{1012}. (right) FIM image of a (1124)-oriented Ru needle specimen. Conditions of acquisition: 45.0 K, 3500 V (~35 V/nm), Main facets identified are Ru{1124} and Ru{1012}. 14

Figure 3.5: Ball model representations of Ru{0001}, {1012} and {1124} selected facets. The atoms composing the first layer (N = 1) are highlighted in red. 14

Figure 3.6: (left) OAP reconstruction of a Ru specimen exposed to $1.2x10^{-7}$ mbar of pure N_2 at 300 K while increasing the static voltage from 2000 to 2500V. (right) Mass spectra of the Ru specimen surface.....15

Figure 3.7: (A) FIM characterization of a Ru specimen and (B) its corresponding OAP heat maps once exposed to 1.2x10-7 mbar of pure N_2 at 300 K while applying a constant electric field on the surface of 13.2, 14.0, 14.7 and 15.1 V/nm. 15

Figure 3.8: Mass spectra of Ru specimen exposed to $2.5x10^{-7}$ mbar of N_2+H_2 gas mixture at 300 K.....16

Figure 3.9 OAP heats maps of N_2^{+}, D_2^{+}($^2H_2^{+}$), N^{+} and D^{+}($^2H^{+}$) on Ru specimen exposed to $2.5x10^{-7}$ mbar of N_2+H_2 gas mixture at 300 K overlayed with the corresponding FIM image. 16

Figure 3. 10: (A) QM calculation of N_2 HOMO and LUMO deformation once the N_2 present in an EF perpendicular to the N-N axis. (B) Iso-electrical-potential surrounding the N_2 molecule while applying different intensity of EF (0, 1, 5 and 10 V/Å).....17

Figure 3.11: Iso-electrical field of 0.1, 1 and 10 V/Å surrounding a Ru cluster with/without applying an external electric field of 1.0 V/Å. 18

Tables

No table of figures entries found.

1.0 Introduction

This project aimed at the development of an Operando Atom Probe (OAP) capable of exploring surface chemical reactions at the nanoscale in real-time on complex surfaces with a complete crystallographic network. In this project, we focused our efforts on exploring the possibility of imaging surface reactions with hydrogen, notably involving nitrogen (N_2) and oxygen (O_2) on Ru and Fe, respectively. N_2 dissociation on Ru plays a crucial role in industrial processes, vital for ammonia (NH_3) synthesis—a key product in fertilizers and a promising candidate for energy storage. Fe oxidation is central to the corrosion process of numerous materials and is important for the hydrodeoxygenation (HDO) of bio-oil. In the recent years, novel approaches involving the use of external electric fields (EEFs) are developed to modulate surface reactivity (**Figure 1**). EEFs have been shown to change surfaces electronic structures, enabling reactions such as the dissociation of N_2 under milder conditions and impacting Fe oxidation. OAP is capable to measure surface composition during chemical reactions while applying EEFs. OAP is a technique of choice for exploring these topics.

We have chosen to structure this report in three distinguishable sections. At first we will focus on the work achieved on Fe oxidation and its reaction with H_2, exploring the mechanisms of oxidation in the presence of reactive gases and the role of EEFs in these processes. The second section addresses our effort regarding N_2 dissociation on Ru surfaces and its reaction with deuterium. By investigating the dissociative adsorption of N_2 and its interaction with deuterium under EEFs, this work aims to understand the conditions necessary to drive these reactions at lower temperatures.

Finally, we will present the key technical developments that enhance the experimental capabilities in these studies in these last two years. This includes the development of a new data treatment software for Operando Atom Probe (OAP) analysis, which allows for more efficient and precise interpretation of experimental results. A high-temperature sample holder has been developed to enable operando studies of surface reactions at high temperatures, expanding the scope of the OAP's capabilities. By combining these experimental approaches and technical advancements, this work seeks to bridge the knowledge gaps in the field of electric-field-assisted surface chemistry. The findings will contribute to a better understanding of the impacts of EEFs on surface chemistry with applications in corrosion prevention, catalysis, and energy storage systems.

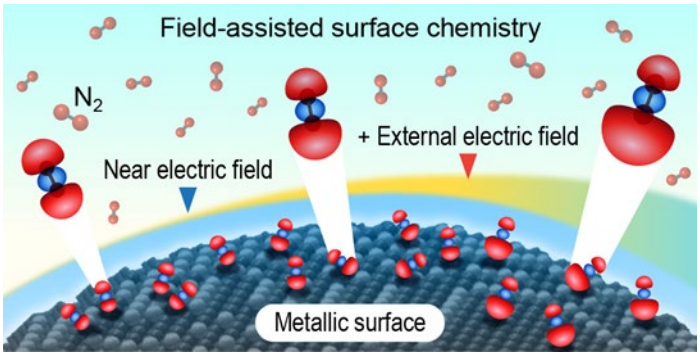

Figure 1: The electronic and chemical properties of a surface are defined by the surface's near-electric field, presenting opportunities to continuously modulate surface chemical properties with an external electric field (EEF). This field-assisted surface chemistry approach uses EEFs to deform N_2 molecular orbitals and enable their dissociation at room temperature on inexpensive and abundant metals.

2.0 Elucidating the Role of Electric Fields in Fe Oxidation via Environmental Atom Probe

Heterogenous catalysis is a surface process involving a complex synergy between the reactants and the surface on which they are reacting. Surfaces' structures and composition evolve while exposed to different reactants, which changes their relative reactivity to those same reactants. A better understanding of those mechanisms at the nanoscale is required to deploy a more systematic and informed catalyst design. Atom probe microscopy techniques are capable to create atomic scale imaging of complex surfaces mimicking the structure of single hemispherical nanoparticle with catalytic properties starting back to the development of field emission microscopy (FEM) and field ion microscopy (FIM) to observe surface reactions in real-time.[1,2,11–13,3–10] However, neither FEM or FIM propose an easy chemical characterization of the surface composition. Atom probe tomography (APT) is capable to image material with an atomic resolution but also propose a more direct identification of those atoms with the use of time-of-flight mass spectrometry. APT is usually performed at cryogenic temperatures in ultra-high vacuum. Our efforts are focused to extend the capabilities of APT to function at ambient temperature and in presence of reactive gases to demonstrate the possibility of observing surface reactions at the nanoscale, a new approach baptized operando atom probe (OAP). However, this OAP imaging process requires the use of intense electric fields (EFs) that will impact the surface reaction. In this specific section we will present the results obtained to monitor the oxidation of a Fe model nanoparticle at the nanoscale in real-time in presence of EFs.

Fe is an abundant element with a great potential for the hydrodeoxygenation (HDO) of bio-oils.[14–16] Understanding how EF affects its oxidation dynamics will provide fundamental insights into mitigating this reaction, which often negatively impacts catalytic properties. [14–16] From a fundamental standpoint, a chemical reaction involves the redistribution of electrons between materials, a redistribution of electric charge in space, and the involvement of strong electric fields. A great number of recent investigations reveal the importance of EFs in surface reactions and propose to consider them as key parameter to characterize them[17–23]. EFs over 1 V/nm can alter reactants' molecular orbital energies, adsorption structures, vibrational frequencies and oxidation states[21,23,24]. This electronic re-distribution completely changes the chemical properties of the reactants and of the surface on which they are reacting. OAP typically works with EFs of the order of 1 to 60V/nm and is subsequently well designed to conduct such studies. In this work we present the EFs effect on O_2/Fe system with the combination of FIM and OAP. All experiments have been conducted at 303 K and with pressures of pure O_2 ranging between 10^{-9} and 10^{-7} mbar. FIM is used to characterize the surface structure of the model Fe nanoparticle while OAP is used to monitor the surface composition during the O_2 exposure. Experimental observations are compared with theoretical models. This work has been achieved in collaboration with Mark G Wirth, Daniel E Perea and Eric VO on the PNNL side; with the Prof. Jean-Sabin McEwen group from Washington State University, notably with Isaac Onyango and Naseeha Cardwell; Prof. Yong Wang (WSU), Prof. Thierry Visart de Bocarme and Prof. Pierre Gaspard from Universite Libre de Bruxelles in Belgium.

2.1 Specimen preparation and FIM characterization

2.1.1 Fe specimen preparation

Fe specimens were prepared from a pure Fe wire (99.9%, Ø ~ 0.1 mm) with an electrochemical etching approach using two different electrochemical etching stages. [25–27] The first etching stage uses a 25% perchloric acid (70%) in glacial acetic acid solution with 10-25 VDC. The second

etching stage uses a 2% perchloric acid (70%) in 2-butoxyethanol with a 10-25 VDC voltage[25]. Prior the electrochemical etching, the Fe wire is cleaned by soaking it in pure phosphoric acid for 20 min. The specimen is cleaned by field evaporation with an initial APT analysis until that the surface presents the field evaporation of pure Fe.

2.1.2 Field Ion Microscopy

FIM is an imaging technique that characterizes the surface structure of materials prepared as sharp needles with atomic lateral resolution (~0.2 nm). The images produced by FIM result from the ionization of imaging gas atoms, in our case Ne, over surface atoms of the positively biased substate surface (i.e. Fe needle). This ionization is made possible by the application of a relatively intense external electric field (EF) on the surface (~35 V/nm) The final FIM image gives a near stereographical projection of the apex on which surface facet structures can be identified by their Miller indices with the condition of having a relatively defect-free surface. In this work, the FIM images were obtained with a LEAP 4000X-HR Local Electrode Atom Probe System commercialized by CAMECA instruments. Data collection and analyses are performed using CAMECA's Integrated Visualization & Analysis Software (IVAS) version 3.8.8.

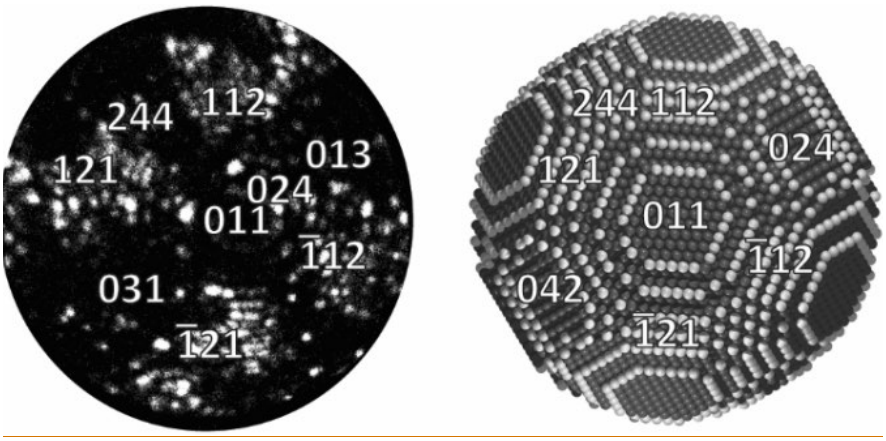

Figure 2.1 (A) FIM image (left) and associated ball model (right) of a (011)-oriented Fe needle specimen. Conditions of acquisition: 45.0 K, 3300 V (~35 V/nm), P(Ne) = 2.2×10^{-6} mbar. Main facets identified are Fe{112}, Fe{013}, Fe{244} and a central Fe(011).

Figure 2.1 shows a (011)-oriented tip. The central (011) pole is surrounded by two pairs of {013}, {024} and {244} facets, and four {112} facets. Fe{112} facets are distinguishable on the FIM image while the other structures remain widely dark. Note that such a field emitter needle tip morphology approximates a single nanoscale catalytic grain where a variety of facets are simultaneously exposed and analyzed as can be seen through the comparison to the ball models.

2.1.3 Atom Probe Tomography, field evaporation cleaning and electric field estimation

While the Fe field evaporation is 33 V/nm at 0 K, this value will decrease at high temperature.[26–28]To estimate the field evaporation of Fe at 303 K, we compare the voltages required to extract Fe ion from the specimen at 45 K and at 303 K. The applied voltage has a linear relationship to the applied electric field and inversely linear to the radius curvature of the specimen: $V_{applied\ voltage} \propto \frac{F_{field\ evaporation}}{R_{curvature}}$.[3] Hence, if the radius curvature does not change significantly

between the two measures, we can infer the value of the field evaporation at 303 K: $F_{303K} = \frac{F_{45K}V_{303K}}{V_{45K}}$. As expected, the voltage at 303 K is systematically lower than at 45 K. As shown on Table 1, the electric field required to field evaporate Fe is systematically lower at higher temperatures. Our experimental datasets enable us to estimate the evaporation field of Fe to 24.8 V/nm at 303 K, which is consistent with Kingham plots reporting the relative mass/charge ratios of different element over the intensity of electric fields.[26,29,30]

2.1.4 Field-assisted Fe oxidation Model

2.1.4.1 Field-Dependent Adsorption Energies

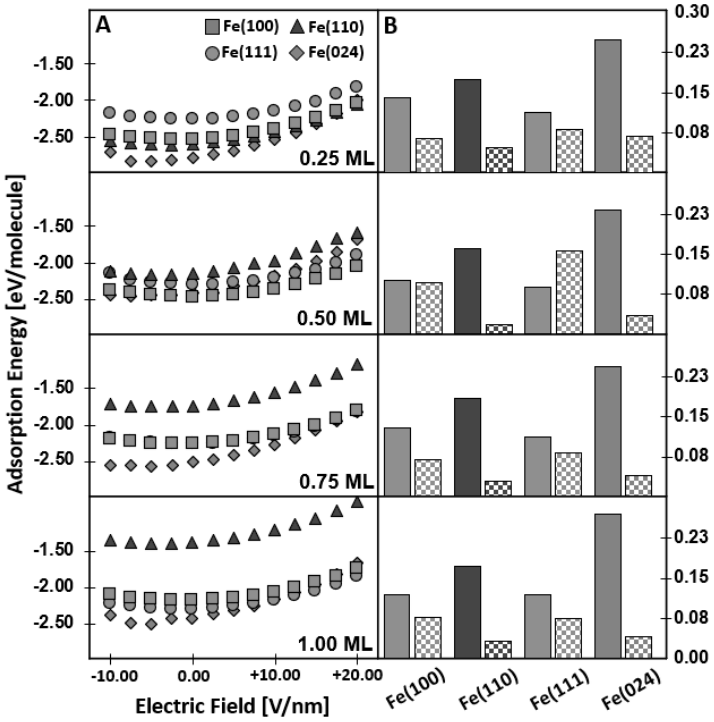

Figure 2.2: (A) Calculated E_{ads} of oxygen atoms on iron at the different coverages for the four facets. The electric field was varied from -10.0 V/nm to +20.0 V/nm in increments of 2.5 V/nm. (B) Changes in Eads by application of a positive 10.0 V/nm (solid bar) or negative 10.0 V/nm (checkered bar) electric field. Changes are in reference to no electric field applied. All coverages tested.

To understand how the EF can influence Fe reactivity, density functional theory calculations (DFT) calculations of the energies of adsorption (E(ads)) of oxygen atoms on the four main Fe facets: (001), (110), (012) and (111). With the general assumption of a negligeable activation barriers between the precursors and the chemisorbed state, four levels of coverage were studied as a function of an applied EF between -10 and +20 V/nm (**Figure 2.2A**). We observe: (1) the E(ads) varies as a parabolic function of the applied EF, consistent with literature findings[16]; (2) besides for the (024) facet, the most negative E(ads) is found at 0 V/nm, indicating that EFs acts against oxygen adsorption on Fe and Fe oxidation; (3) the EF seems to impact compact facets like Fe(011) more than more open facets like Fe(111). To have a better impression of how EF impact those E(ads) we have calculated E(ads) differences from no-EF applied to the application of

positive and negative EF (-10 and +10 V/nm respectively), shown in checked and solid bars respectively. (**Figure 2.2B**). Our calculations show that a positively biased EF has a greater impact of the E(ads) than a negative one, regardless of the oxygen coverage value. Fe(111) exhibits the smallest change with positively applied fields and largest change with negatively applied fields, which indicates that positive and negative EFs have differing effects on lateral interactions in these O/Fe systems.

2.1.4.2 Spatial-time conversion and constant electric field

OAP consists of performing an APT analysis at constant voltage while exposing the specimen to reactive gases – oxygen in this current work. In OAP, a constant DC EF is applied near but below the field evaporation threshold of the Fe substrate while still strong enough to induce oxygen adsorption, and a pulsed EF is periodically applied to provoke the field evaporation surface species, allowing to probe the surface composition. An OAP result is a 3D atom map but in a "(x,z,t)" space instead of a "(x,y,z)" space for APT. An OAP atom map can be seen as the surface composition of the specimen over time. But thhis approach requires to make important approximations: (1) The quantity of surface atoms removed does not heavily impact the global geometry of the substrate such that it conserves its radius curvature and its realtive crystallography; under an evaporated Fe(011) facet, there it a new Fe(011) facet. (2) The radius curvature of the specimen does not change enough to allow global applied EF to remain unchanged if the applied voltage is constant.

The oxygen concentration heat maps, reported in **Figure 2.3A** as the proportion of O atoms detected vs the total amount of collected atoms, indicates the heterogenous distribution of Fe oxides over specific faceted regions of the Fe surface. O atoms are mainly detected in the form of Fe_2O^{n+} and FeO^{n+} ions (with n=1,2) found at 64 Da and 72 and 36 Da. Besides Fe_2O^{n+} and FeO^{n+}, O^+ detected at 16 Da may be the result of straight field evaporation of surface O atoms or from the post-field dissociation of field evaporated O_2 into atomic oxygen species. After 30 min of exposure, O atoms are found more on open facets like Fe{112} and Fe{244} than on compact facets like Fe{013} and Fe{011}, (**Figure 2.3B**), clearly showing experimentally wich facets are more prone to initiate oxide formation, which is consistent with the previous observation fof G. Cranstoun and J.T. Lynch with FIM.[4] .

To compare the experimental results with our first principles-based model, Kubic Harmonics[31] were used to expand the E(ads) of oxygen on a multifaceted Fe surface. The tip was modeled with a hemispherical geometry with a EF strength varying decreasingly from the top of the apex towqards the shank. The normalized surface oxygen distribution on the Fe apex was simulated over a period of 18000 seconds with an oxygen pressure of 1.1×10^{-8} mbar.[31]

Orinigally, plots constructed using adsorption energies presented in **Figure 2.2** were qualitatively agreeing with experiment but the electric field and temperature (30.5 V/nm and 700 K[31]) for the simulations drastically differ from experiment (~24.8 V/nm and 303 K). Note that our original calculation were not taking into account the formation of a Fe oxide layer, which we found to already be present at the start of the experiment, and so the overall oxygen adsorption strength is likely overestimated. With an adsorption energy uniformly reduced by 1.2 eV across all crystal facets during the construction of the multifaceted plots, the parameters (24.12 V/nm and 303 K) align well with those used in the experiment (**Figure 2.3**). The corresponding local oxygen coverage over the Fe surface is displayed at different timeframes in **Figure 2.3C** and compared to the experimental findings in **Figure 2.3A**. As can be seen from the plots, there is a depletion of the oxygen coverage around the {024} facets while there is a high oxygen coverage as one approaches the {013} facets as one approaches the flanks of the tip. The decrease of the oxygen

coverage around the {024} correlates well with the fact that the oxygen binding energy decreases significantly on this facet in the presence of a positive field. Experimentally, we find that the formation of an oxide occurs over Fe{244} while the Fe{013} facets remain oxygen-free.

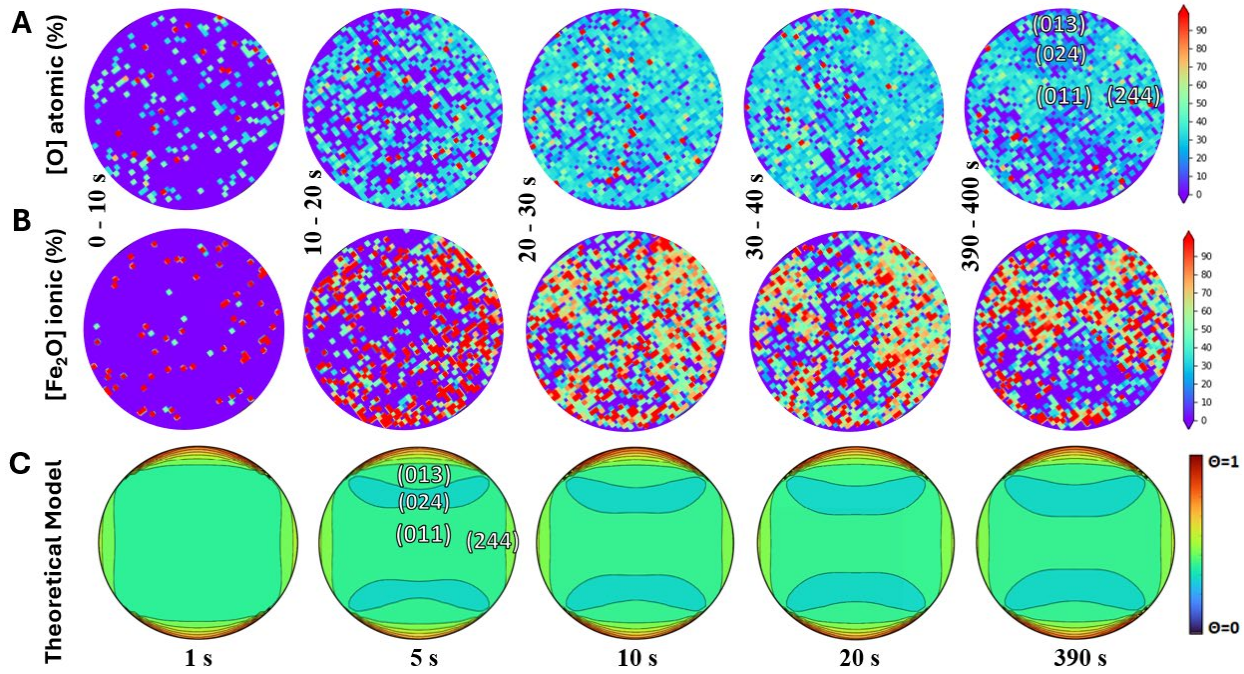

Figure 2.3: Experimentally measured 2D projection composition maps of (A) O(%)atomic, (B) Fe_2O^{n+}ionic of a Fe specimen exposed to 1.2×10^{-7} mbar of pure O_2 with a constant 15 V/nm (24.8 V/nm pulsed) applied EF at room temperature. The experimental composition maps shown are displaying the average composition detected over a 5 min time lapse (C) Theoretically derived 2D projection composition maps from corresponding first principles-based model of evolving oxygen coverage over a field emitter tip with an EF of 24.12 V/nm, a pressure of 1.1×10^{-8} mbar and a temperature of 300 K.

OAP offers the possibility to study chemical phenomena under intense EFs. Applied EFs impact chemical systems in multiple ways promoting or inhibiting a given reaction pathway.

2.1.5 Differential adsorption of $^{2}H_2$ and $^{18}O_2$ on Fe in presence of electric field

In the attempt to observe a surface reaction, a Fe specimen is simultaneously exposed to pure $^{18}O_2$ and $^{2}H_2$ gases at room temperature in presence of an electric field estimated at ~15 V/nm.

While applying a constant voltage, we added the reactive gases sequentially. The $^{18}O_2$ was added first, until the pressure detected reaches $5x10^{-7}$ mbar. The $^{2}H_2$ was then added in the chamber until that the detected pressure reaches $7x10^{-7}$ mbar. The pressure gauge of the LEAP5000 has a sensitivity 2.4 times higher for $^{2}H_2$ than for $^{18}O_2$. Consequently, the actual pressure of $^{2}H_2$ is close to $4.8\ x10^{-7}$ mbar, which makes us reach stoichiometric proportion of $^{2}H_2$ and $^{18}O_2$.

The massive increase of background noise was observed with the presence of hydrogen in the chamber (The mass spectra is reported in **Figure 2.4**). The possible cause would be that hydrogen uncontrollably ionizes on the microchannel plate composing the detector. However, this

observation has been only made on specimen warmed at room temperature, which leads us to think that the hydrogen acts as a field evaporation trigger. The use of hydrogen and oxygen isotopes allows us to observe the presence of native contaminations. ^{1}H is still observe as a natural contaminant in any UHV system while ^{2}H and $^{2}H_2$ are observed at 2 and 4 Da. Additionally, ^{2}H is also detected associated with Fe. Remaining ^{16}O is detected at 16 Da but not at 32 Da in the form of $^{16}O_2$. We conclude that those O atoms are native contaminant present in the Fe specimen. On the opposite, ^{18}O atoms are detected combined with Fe in the form of $Fe_2{}^{18}O$ and $Fe^{18}O$, but also $^{18}O_2$ confirming that most of Fe oxides result of the reaction with the $^{18}O_2$ gas added in the chamber.

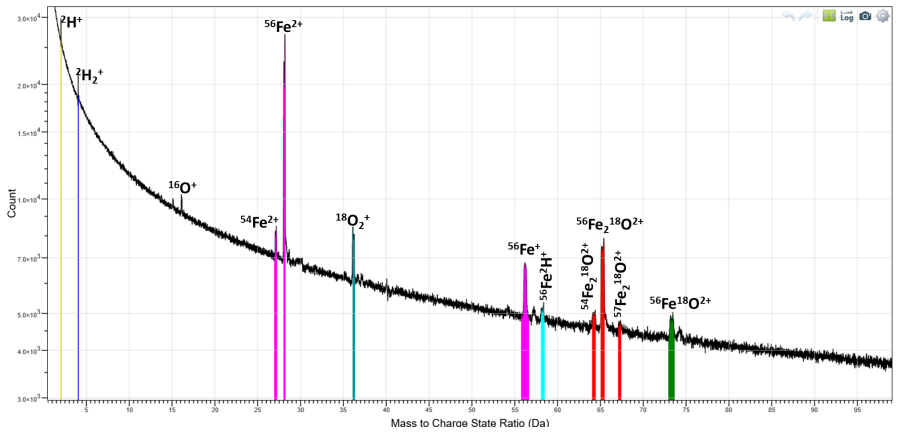

Figure 2.4: Mass spectra of a Fe specimen exposed to ~1x10^{-8} mbar of $^{2}H_2$+$^{18}O_2$ (1:1) gas mixture at 300 K while applying ~15 V/nm on the surface.

The resulting OAP reconstruction reveals that ^{2}H and ^{18}O are preferentially found on specific regions of the Fe surface. These regions are identified by superposing the surface map obtained by FIM (**Figure 2.8**). While ^{2}H is mainly detected over Fe (011), {024} and {013}, the ^{18}O is mainly localized on the Fe{112} as previously found in Fe oxidation experiments.

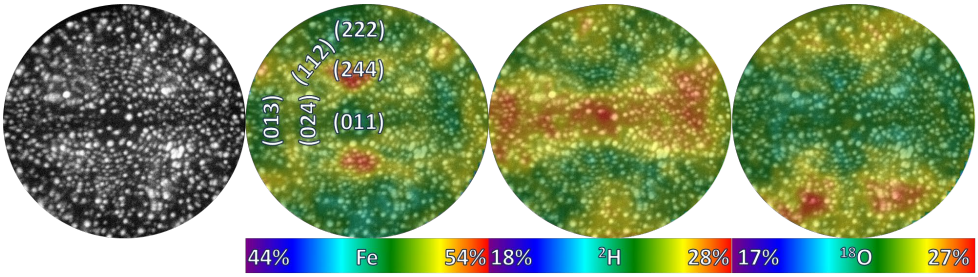

Figure 2.5: FIM characterization of Fe specimen, and its surface composition found by OAP while exposed to ~1x10^{-8} mbar of $^{2}H_2$+$^{18}O_2$ (1:1) gas mixture at 300 K while applying ~15 V/nm on the surface.

^{2}H and ^{18}O are detected in different regions of the surface, but no potential products of reaction between the two are found. This could be due to the relatively low temperature of the system (300 K) but it is mostly probably due to the very intense electric field present on the surface at high frequency (100 kHz), leaving not enough time for the adsorbed atoms to diffuse and eventually react. While more exploration is necessary, a different application of the electric field must be considered, notably by applying electric pulses at low frequency, a feature that require an important setup modification only possible with the assistance of the vendor.

2.1.6 Normalized Oxygen Distribution on the Fe Surface

The oxygen distribution was simulated at 20, 24.12 and 25 V/nm (**Figure 2.6A-D**) – these values were chosen as they are close to the experimentally tested range of applied EFs. In theh 20 V/nm case, starting from a relatively free-oxygen Fe surface, the surface is rapidely covered by oxygen after 10 s of exposur with a lower coverage over the central Fe(011) compared to the peropherical regions. The distrbution is relatively concentric, reflecting our modelization of the EF over the hemipsherical shaped specimen with a higher EF on the central apex and a lower EF on the shank. Note that the coverage around the Fe{024} and Fe{013} facets is less as compared to the Fe{244} facets as is seen with the OAP observations. Open facets such as Fe{244} are particularly responsive to oxygen adsorption as compared to high-coordination Fe{024} facets. Hence, larger oxygen coverage is expected over Fe{244} as compared to Fe{024}. At 20 V/nm and 24.12V/nm, such a decrease in the oxygen coverage on the Fe{011} is not observed in our multi-faceted Fe grain model. This is likely due to the field-induced higher oxygen partial pressure at the apex of the tip than at its periphery.

The heterogeneous distribution of the O coverage influence by the surface structuyres can start to be seen with an applied EF of 24.12 V/nm. In this case we can see that the O coverage is relatively more important on the Fe(011) central facet, the Fe{013} facets and the Fe{244} facets, while the Fe{024} has relatively less O. Finally, at 25 V/nm, we see that the overall coverage decrease even more and the equilibrium is reached after less than 1 second of exposure.

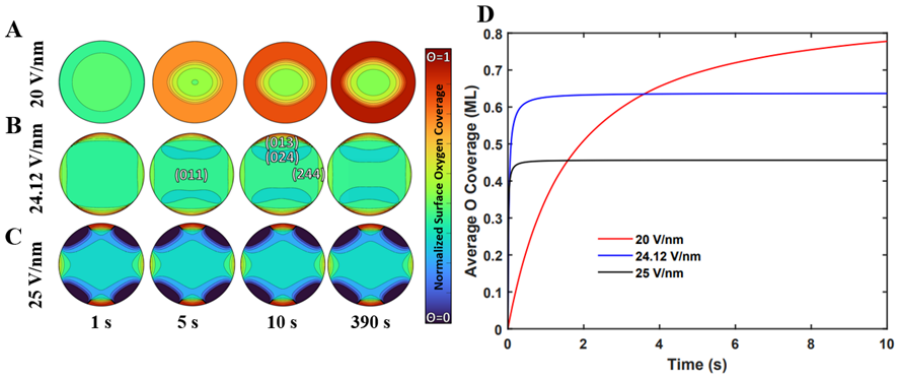

Figure 2.6: Snapshots of the time evolution of oxygen coverage on the Fe crystallite at 1.1×10^{-8} mbar and 700 K under (A) 25 V/nm and (B) 30.5 V/nm applied electric fields. (C) Time evolution of oxygen coverage under varying electric fields with the inset highlighting the first 60 seconds. (D) Snapshots of the time evolution of oxygen coverage on the multifaceted crystallite for the first 10 seconds in the presence of an electric field of 30.5 V/nm.

The oxygen coverage pattern appears earlier and corresponds to the OAP observations with high oxygen coverage on the Fe{244} and lower coverage over the Fe{013}(**Figure 2.3A**). From **Figure 2.6D**, we see that the 24.12 and 25 V/nm-cases reach equilibrium faster than the 20 V/nm case, indicating higher oxygen adsorption rates for higher EFs while the equilibrium oxygen coverage decreases, as observed experimentally. Those models are consistent with OAP observation and translate the effect of EFs on partial pressure by polarizing and attracting gas molecules towards the surface[16]:

$$P_{O_2}(F) = P^0_{O_2} e^{\beta \alpha_{O_2} (\frac{F^2}{2})}$$

Pressure enhancements at the apex of the tip for the 20, 24.12 and 25 V/nm EF correspond to 5.4×10^{-5}, 2.7×10^{-3} and 6.7×10^{-3} mbar, respectively. The enhancement at the border of the field of view for 20, 24.12 and 25 V/nm EF are 3.9×10^{-5}, 1.7×10^{-3} and 4.2×10^{-3} mbar, respectively. The pressure enhancement is not uniform due to disspating electric field strength away from the tip of the hemisphere. Oxidation occurs rapidely with 24.12 V/nm (**Figure 2.6D**), we observe that the 4-fold symmetric distribution starts at 5 s with distinct separated zones of oxygen coverage. At 10 s, we see the oxygen coverage pattern consistent with that observed at equilibrium, forming a model that is highly compatible with experimental data. This early development shows how the system is sensitive to initial conditions. Calculated oxygen coverages are higher than 0.6 ML while the oxygen coverages measured by OAP is ~0.3 ML. This deviation can be attributed to the out-of-equilibrium nature of the OAP approach - constantly removing totally or partially the adsorbates from the surface. Ultimately, intense EFs as high as 40 V/nm completely prevent the interaction of the Fe(011) with oxygen.

The theoretical EF of 24.12 V/nm results show close agreement with OAP observations. However, the theoretical model is also limited due to the difficulty of explicitly modeling subsurface oxygen for every facet. The experimental model also detects oxygen ions present in the system rather than oxygen coverage on the Fe grain, as the theoretical model does. Regardless of the limitations of our model, the correlation between our models and the experimental results gives us fundamental insights into effects of electric fields on surface oxidation and how one can control the oxidation state of the metal in their presence. We also note that the inclusion of the fourth facet is crucial in our multi-scale model. Without the inclusion of the {024} facet, one would not get the oxygen depletion zones around the Fe{024} and the Fe{013} as seen experimentally. The inclusion of this fourth facet in our model was informed by experiment. Our work therefore demonstrates the critical need for a feedback loop between experiment and theory that enables the development of predictive models for such complex systems. The influence of hydrogen on the oxidation mechanism has been observed in other systems, notably Mg[32], W[33] and Fe[4], where intentially added hydrogen is shown to promote of field evaporation at lower applied EFs. In our case, no hydrogen nor water has been intentionally introduced in the APT system, but their presence is irrefutable and probably unvoidable. In the future, it will be necessary to include the influence of H and H_2O in future models.

2.2 Conclusion and perspectives

In this work, we successfully demonstrated the capabilities of Operando Atom Probe to observe Fe oxidation under the action of high EF in real-time. OAP observations highlight the effects of surface structures, showing that the Fe oxidation primarily occurs on open facets like Fe{244} and Fe{112}, while high-coordination facets like Fe{024}, Fe{013} and Fe{011} remain relatively immune to the initial stages of oxidation. OAP experiments supported by DFT calculations and a mean-field model on a multi-faceted catalytic grain, combined with statistical-mechanical considerations, lead to the same conclusion: intense EFs have strong influences on Fe oxidation by polarizing and attracting gas molecules towards the surface, increasing de facto the local pressure through a local electric field enhancement at the apex of the tip. [16,21,22,24,34–36] Excessive EFs mitigate Fe oxidation by the occurrence of field evaporation and a decreased oxygen binding strength to the surface as elucidated through our DFT-based model. Additionally, through simple modifications to modern APT systems, OAP can help facilitate unique experiments to provide fundamental insight into electric field enhanced chemical reactions. Furthermore, further development utilizing Kingham plots will lead to more accurate measurements of localized electric fields, which will be the subject of further studies. Due to the physical nature of those effects, it is reasonable to think that they can be extrapolated to a broad range of chemical systems and open a new perspective of how one can dynamically influence a given reaction of interest with EFs.

3.0 Tracking N_2 field-assisted dissociation on Ruthenium and Iron by Operando Atom Probe

Nitrogen (N_2) plays a key role in global food production as the primary precursor for ammonia (NH_3), a critical component in fertilizer production. When combined with renewable sources of electricity, NH_3 presents a promising alternative for energy storage.[37–39] However, those promising applications are vastly limited by the difficulty of activating N_2 reactivity [40,41]. Despite the use of catalysts, N_2 chemical conversion requires high-temperature operation to overcome its inherent stability. A novel approach involves using external electric fields (EEFs) to finely tune the local electronic environment of a surface and continuously alter its chemical properties. This enables even cheap and abundant metals to dissociate N_2 at room temperature. From a fundamental standpoint, the reactivity of a metallic surface with a molecule is determined by the interaction between the electronic states of the molecule and the metal surface. A chemical interaction is an electronic interaction, making it sensitive to the presence of electric fields.

Electric fields can alter the thermodynamics of chemical reactions in a manner similar to temperature and pressure. A van't Hoff equation can be constructed in which the effect of the field is described as a function of the new electric moment (electric dipole moment, polarizability). As predicted by Oppenheimer, the application of intense electric fields higher than 1 V/nm can trigger drastic alterations of the chemical system and change the energies of molecular orbitals and adsorbates, thereby altering the activation barriers for adsorption, desorption, dissociation, diffusion, and their associated kinetic parameters, resulting in a field-assisted mechanism. While the effects of electric fields on reaction thermodynamics have been extensively investigated by Debye and Bergmann, the classical electrostatic approach does not apply to intense fields. Fields higher than 10 V/nm cause significant atomic/molecular orbital energy shifts, changing chemical properties and resulting in the emergence of new reaction pathways. Kreuzer et al. propose quantum mechanical approaches to reveal the new physics and chemistry in high electrostatic fields.

The first emergence of these high electrostatic fields came with the development of Field Ion Microscopy (FIM). FIM consists of field emitter tips with the apex sharpened to a radius on the order of a few tens of nanometers. A positive voltage of several kilovolts is applied to a counter-electrode to create an intense electric field in the vicinity of the apex. An imaging gas, usually helium, neon, or argon, is introduced into the vacuum chamber. The gas atoms approaching the apex are polarized and accelerated to the surface in the inhomogeneous field before hitting the surface, where they are ionized and repelled from the positive surface toward a detector screen to produce a nanoscale image of the surface. The electric field intensity obtained in FIM, as high as 40 V/nm, can polarize and attract helium atoms and force their adsorption onto the surface at low temperatures, with a binding energy of 0.4 eV, 100 times higher than the binding energy in the absence of a field.

Observing drastic changes when intense electric fields are applied, M.L. Karakha and H.J. Kreuzer focused on the effect of strong electrostatic fields on diatomic molecules such as N_2. Their calculations revealed that the field can reconfigure the electronic distribution of N_2 such that one N atom behaves chemically like a C atom, while the other N becomes O-like. The binding energy of N_2, which is 9.7 eV in zero field, increases to 11.0 eV in a field of 62 V/nm, corresponding to the CO binding energy at zero field. While the chemical properties of matter are determined by discrete electronic states, the addition of an EEF results in field-induced chemistry, continuously altering the chemical characteristics of one element relative to another (Figure 3.1).

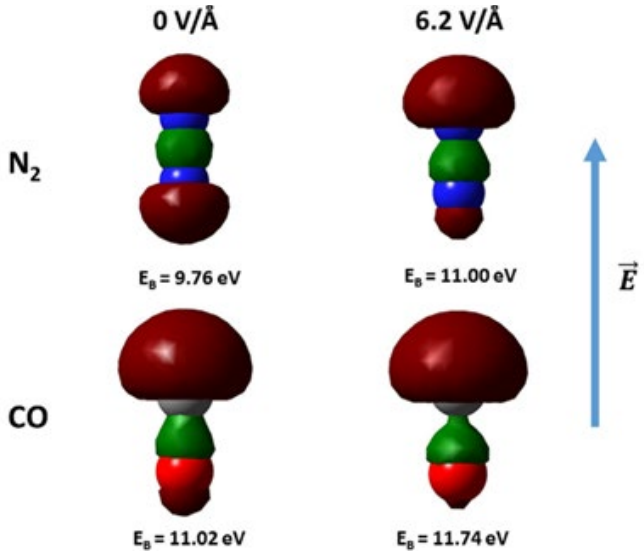

Figure 3.1: Electronic bonding (green) and anti-bonding (burgundy) orbitals for N2 (N blue) and CO (C gray, O red) in zero field and in 62 V/nm[21].

In their attempt to develop needle sharpening methods for Field Ion Microscopy (FIM) and Atomic Force Microscopy (AFM), M. Rezeq, J. Pitters, and R. Wolkow demonstrated the possibility of triggering N_2 dissociation on W surfaces at temperatures as low as 100 K [13,25,42](**Figure 3.2**)The field adsorption of N_2 on W can lead to the formation of "strong-bond" states arising from N_2 dissociation on W, followed by N diffusion within the first W atomic layers. This diffusion causes the formation of W atom protrusions, triggering the field evaporation of surface W atoms.

In this study, we observe the first limit of EEF usage. While applying a strong field to the hemispherical W surface, several phenomena occur simultaneously. Even before N_2 approaches the surface, an excessively high EEF can trigger the field evaporation of the surface—a phenomenon that can be described as the rupture of surface atoms as ions under a particularly intense electric field. This natural phenomenon is used in APT to probe and collect the atoms composing a needle-shaped specimen. While most pure elements have specific, determined values for field evaporation, the mechanism remains largely unexplored.

As N_2 approaches the surface, it can directly ionize via tunnel effect under the action of strong local electric fields. N_2 dissociative adsorption only occurs in relatively low-field regions where it can penetrate the ionizing barrier. A "nitro-corrosion" mechanism has also been observed at low temperatures (<100 K) on Ir and Pt by E.W. Muller and J.F. Mulson.[42]

Overall, there is a strong consensus confirming the positive action of the electric field on N_2 activation and dissociation on metallic surfaces. Despite N_2 being one of the most stable and strong chemical bonds in nature, the presence of a sufficiently strong field can polarize the N_2 molecule, impose a dipole moment, change the electronic envelope of the nitrogen nuclei, and influence how the N_2 molecule approaches the surface. In this section, we propose to present the first experiments using Operando Atom Probe (OAP) to explore the possibility of dissociating N_2 on the surface of Ru. The OAP will be used to determine the intensity of the electric field at which N_2 dissociation is detected.

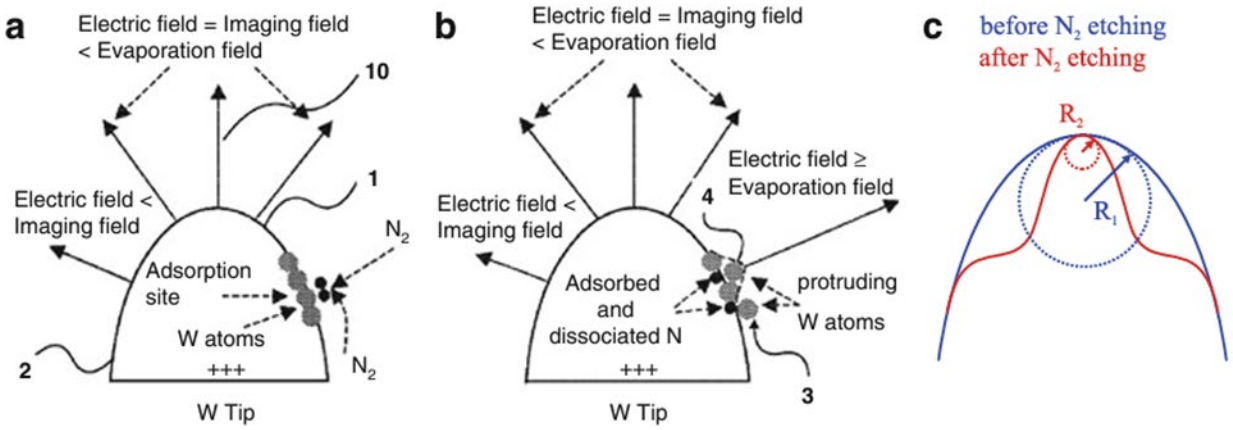

Figure 3.2: Schematic description of the sharpening process. (a) N2 can only adsorb to the tip shank where the field is lower than at the apex. (b) The W-N bond weakens the bonding of the W atoms to the tip, and they field evaporate, leading to a preferential loss of material around the tip shank. (c) Tip profile before etching (blue), and after (red), illustrating a reduction in local radius of curvature at the apex and the final "shouldered" shape of the tip[13].

3.1 Methods

3.1.1 Field Ion Microscopy characterization of Ruthenium

Ru specimens were prepared from a pure Ru foil using a Plasma Focused Ion Beam, which allows thinning the specimen with a Xe beam. The specimen is cleaned by field evaporation in the APT, with an initial APT analysis conducted until the surface presents the field evaporation of pure Ru. At 45 K under UHV conditions, Ru is primarily detected in the form of $^{96}Ru^{2+}$, $^{98}Ru^{2+}$, $^{99}Ru^{2+}$,$^{100}Ru^{2+}$, $^{101}Ru^{2+}$, $^{102}Ru^{2+}$, $^{104}Ru^{2+}$, $^{96}Ru^{3+}$, $^{98}Ru^{3+}$, $^{99}Ru^{3+}$,$^{100}Ru^{3+}$, $^{101}Ru^{3+}$, $^{102}Ru^{3+}$, $^{104}Ru^{3+}$ at 48, 49, 49.5, 50, 50.5, 51, 52, 32, 32.67, 33, 33.33, 33.67, 34, 34.67 Da, respectively (**Figure 3. 3**).

Ru isotope	m/z for Ru^{+}(Da)	m/z for Ru^{2+}(Da)	m/z for Ru^{3+}(Da)
^{96}Ru	96	48	32
^{98}Ru	98	49	32.67
^{99}Ru	99	49.5	33
^{100}Ru	100	50	33.33
^{101}Ru	101	50.5	33.67
^{102}Ru	102	51	34
^{104}Ru	104	52	34.67

We also find noticeable peaks at 7 and 14 Da, corresponding to N^{2+} and N^{+}, respectively, and a peak at 16 Da corresponding to a native presence of oxide. The relative abundance of Ru^{2+}/Ru^{2+} at 2.6 allows us to estimate the surface electric field at 41-42 V/nm to collect those Ru ions, with the help of the Kingham plots(**Figure 3.3**).

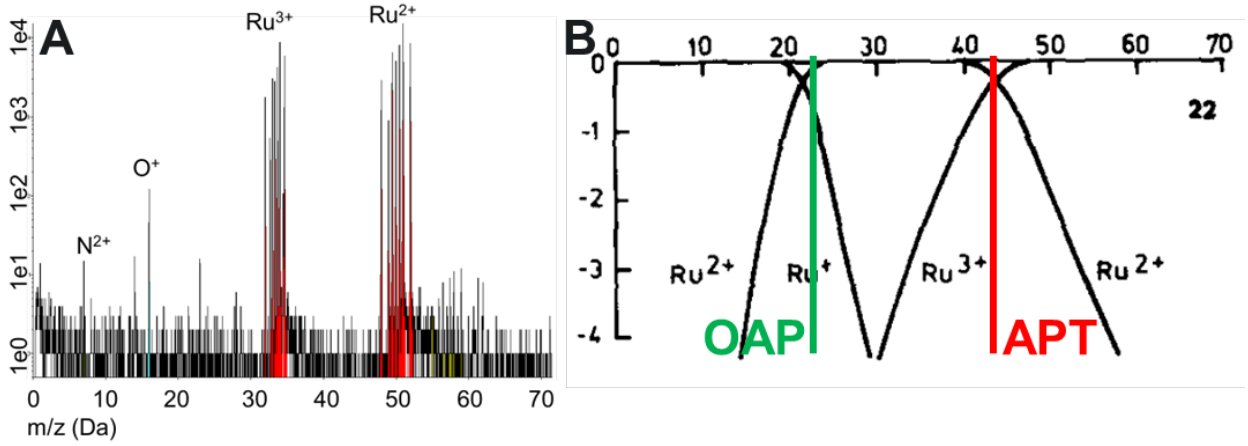

Figure 3.3 (left) Mass spectra of Ru specimen Field evaporation cleaning by APT. (right) Kingham plot of Ru reporting the relative abundance of Ru^{+}. Ru^{2+} and Ru^{3+} depending of the intensity fo the electric field triggering the field evaporation.

FIM is an imaging technique that characterizes the surface structure of materials prepared as sharp needles with atomic lateral resolution (~0.2 nm). The details on the imaging process and instrument can be found in the section 2.1 of this report. FIM relies on the ionization of Ne on the surface of the apex. This ionization requires a certain electric field (EF) intensity, typically 35 V/nm for Ne. This poses a fundamental limit on image quality, depending on whether the surface material will field evaporate before Ne can ionize.

For example, Fe field ionization requires 33 V/nm, meaning the field evaporation of Fe becomes statistically probable as we try to increase the electric field to ionize Ne. As a result, the FIM image of Fe becomes relatively blurred because Fe atoms become unstable when applying 35 V/nm to ionize the imaging gas. This phenomenon is even more pronounced when imaging a material like Ru, where the field evaporation requires at least 41 V/nm, significantly more than Fe. As shown in **Figure 3.4**, the resulting FIM image of Ru is clearer and more stable, facilitating the identification of different surface structures.

Figure 3.4(left) shows a (0001)-oriented tip. The central (0001) pole is surrounded by six {1124} and six {1012} facets (**Figure 3.5**). All facets of those groups are not visible since that the (0001) is slightly ex-centered, making only (1102), (2-1-14), (10-12), (11-24) and (01-12) clearly visible. **Figure 3.4(right)** shows a (11-24)-oriented specimen with a (rare) spiral dislocation defect on its surface (shown with the red arrow). In this specimen, the (0001) is totally out of the field of view while the open (2-1-14), (10-12) and (11-24) facets are in the center. After this careful cleaning and surface structure identification, the specimen is warmed and stabilized at 300 K.

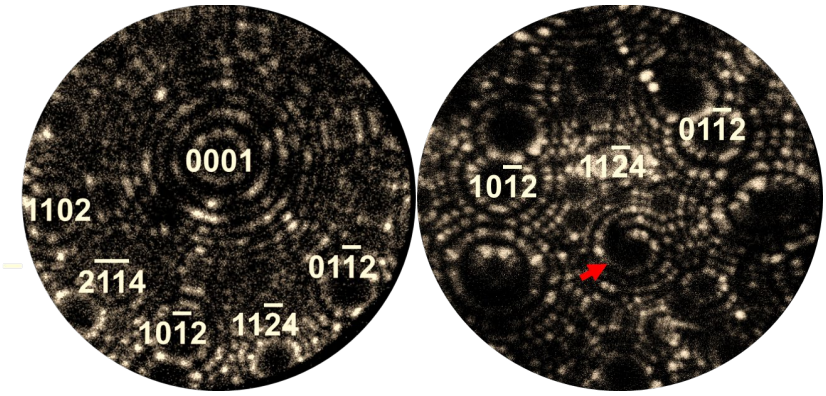

Figure 3.4: (left) FIM image of a (0001)-oriented Ru needle specimen. Conditions of acquisition: 45.0 K, 5500 V (~35 V/nm), Main facets identified are Ru(0001), Ru{1124} and Ru{1012}. (right) FIM image of a (1124)-oriented Ru needle specimen. Conditions of acquisition: 45.0 K, 3500 V (~35 V/nm), Main facets identified are Ru{1124} and Ru{1012}.

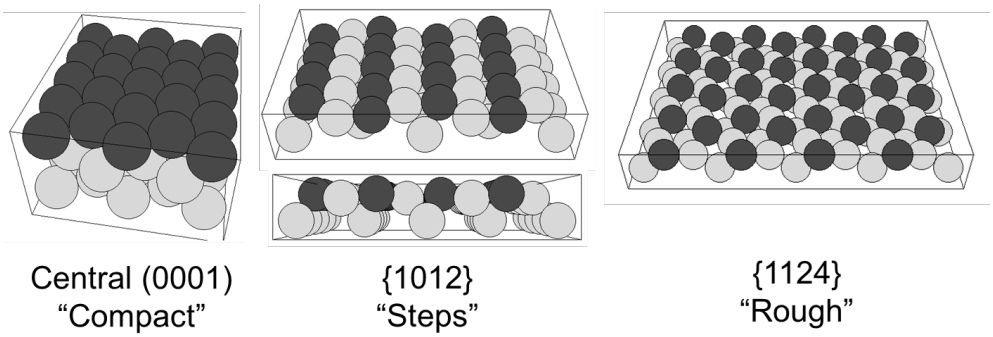

Figure 3.5: Ball model representations of Ru{0001}, {1012} and {1124} selected facets. The atoms composing the first layer (N = 1) are highlighted in red.

3.2 N_2 field-assisted dissociation on Ru

3.2.1 N_2 field dissociation

After thermal stabilization, the Ru specimen is periodically exposed to $1.2x10^{-7}$ mbar of N_2 while maintaining a constant voltage. The goal of this approach is to determine at which applied voltage the presence of N_2 on the surface becomes noticeable. First, a voltage of 2000 V is applied to the specimen for 5 minutes. Then, $1.2x10^{-7}$ mbar of N_2 is introduced into the chamber, where it remains for 5 minutes. Afterward, the N_2 is evacuated from the chamber for another 5 minutes. This process is repeated with increasing voltages of 2000, 2200, 2300, 2400, and 2500 V. The resulting atom probe 3D reconstruction from this experiment is shown in **Figure 3.6**(left). The reconstruction is divided by "voltage" section, from which the heat maps will be calculated.

The presence of N_2 in the chamber inevitably increases the background noise in the mass spectra. N_2 is detected in the form of N^+, N_2^+, and RuN_2^{2+} at 14, 28, and 62-66 Da, respectively. Water contamination is also detected, indicated by the presence of O^+, H_2O^+, and RuO^{2+} at 16, 18, and 56-60 Da, respectively. Interestingly, Ru is detected in the form of Ru^{2+} and Ru^+ (with a ratio of 9:1), instead of Ru^{2+} and Ru^{3+} (**Figure 3.6**(right)). According to Kingham plots (**Figure**

3.3(right)), this Ru^{2+}/Ru^{+} ratio indicates a field evaporation intensity of 22-23 V/nm. By subtracting the portion related to the constant electric pulse of 1314 V, we can deduce the intensity of the constant applied electric field, which ranges between 13 and 15 V/nm.

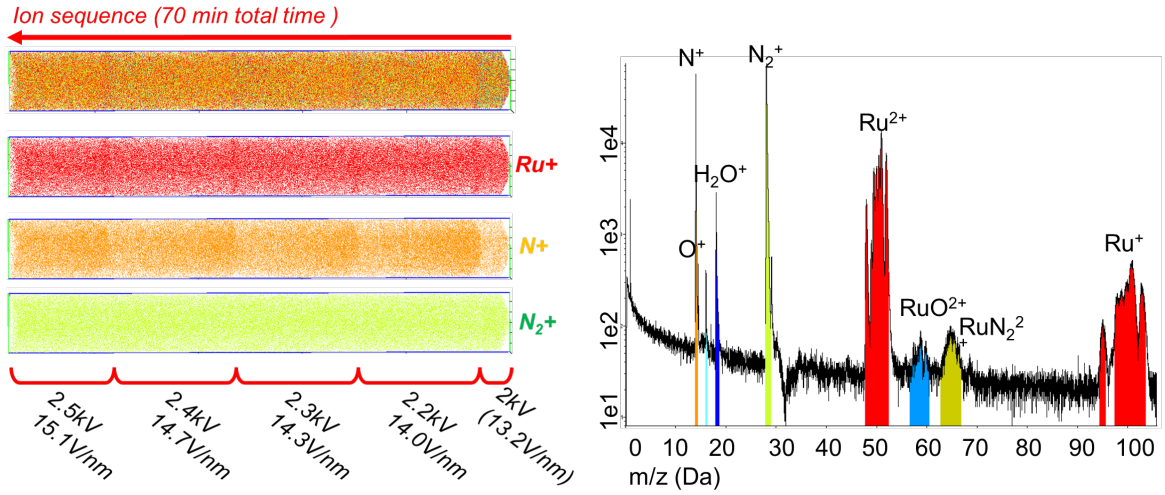

Figure 3.6: (left) OAP reconstruction of a Ru specimen exposed to $1.2x10^{-7}$ mbar of pure N_2 at 300 K while increasing the static voltage from 2000 to 2500V. (right) Mass spectra of the Ru specimen surface.

Heat maps measuring the relative concentrations of N_2^{+} and N^{+} were generated for each voltage section and overlaid with the FIM surface map. These two species allow for distinguishing between the dissociative adsorption and ionization zones. N^{+} is mainly detected over Ru(0001) and Ru{1124}, while N_2^{+} is detected in the zones surrounding these regions. As reported in previous studies, N_2 dissociation is a rate-limiting step, even for Ru[43–45]. While the occurrence to N_2 dissociation has been found on STM at 300 K[45], the probability is fairly low (0.04%). Through OAP experiments, we can confirm the possibility of triggering this rate-limiting reaction at 300 K and estimate the electric field intensity between 13 and 15 V/nm. The next step is to develop models to verify this possibility and estimate the rate of occurrence.

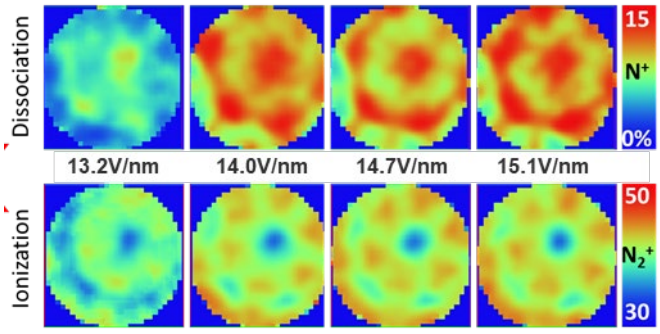

Figure 3.7: OAP heat maps of the specimen shown in Figure 3.1(left) once exposed to $1.2x10^{-7}$ mbar of pure N_2 at 300 K while applying a constant electric field on the surface of 13.2, 14.0, 14.7 and 15.1 V/nm.

3.2.2 Differential adsorption of N_2 and $^2H_2$ on Ru

As previously described in section 2.2.4, the installation of Operando Atom Probe on the LEAP5000 opened the possibility to simultaneously expose the specimen to N_2 and $^2H_2$. The (11-24)-oriented Ru specimen is exposed to a N_2+H_2 gas mixture (1:1) with a total pressure of $2.5x10^{-7}$ mbar. $^2H_2^+$ and $^2H^+$ are both detected at 2 and 4 Da, confirming the dissociation of hydrogen (**Figure 3.8**). However, the presence of hydrogen also increased the background noise. N_2^+ was detected at 28 Da, but N^+ (14 Da) was not necessarily observed. This could either indicate the absence of N_2 dissociation, or it is possible that the background noise obscured the N^+ peak.

Ru being solely detected as Ru^{2+} leads us to conclude that the applied electric field was between 25 and 35 V/nm. Further investigation will be necessary to refine this estimation.

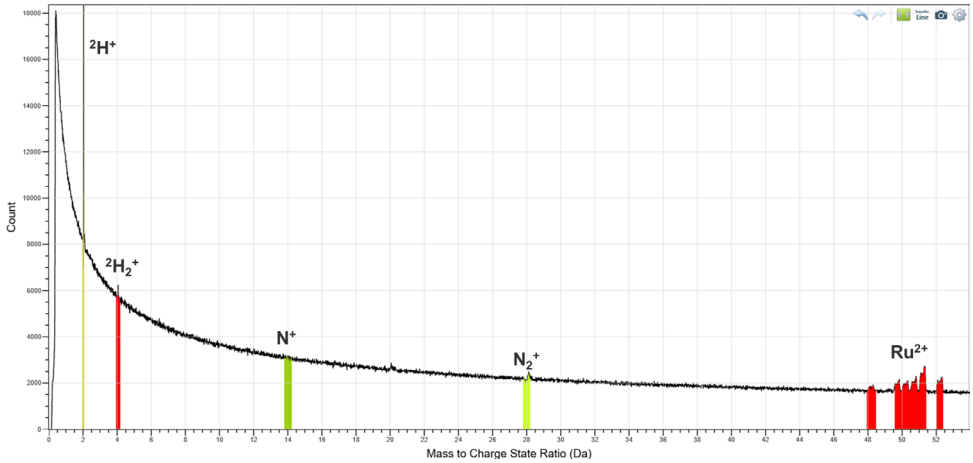

Figure 3.8: Mass spectra of Ru specimen exposed to $2.5x10^{-7}$ mbar of N_2+H_2 gas mixture at 300 K.

OAP heat maps are measured from the atom probe reconstruction of the experiment. N^+, N_2^+ and $^2H_2^+$ are mostly detected in regions nearby the (10-12) – (11-24) – (01-12) axis. On contrary, $^2H^+$ are mainly detected on this axis as depicted on **Figure 3.9**.

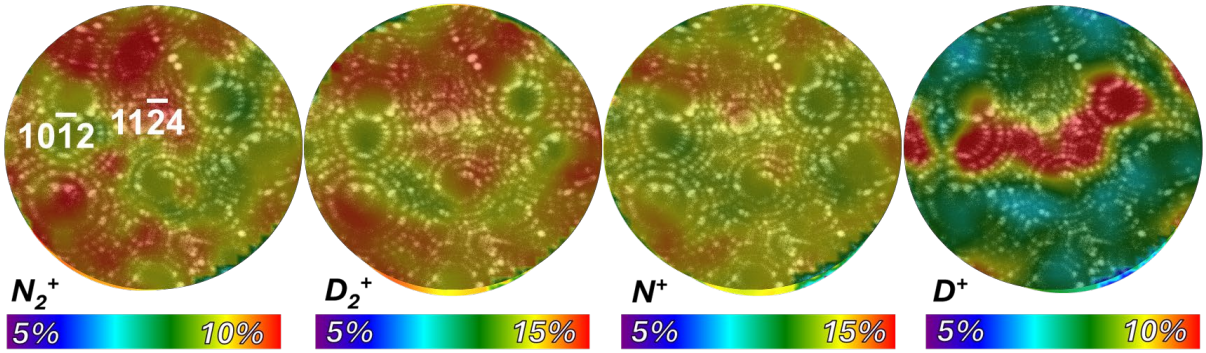

Figure 3.9 OAP heats maps of N_2^+, D_2^+($^2H_2^+$), N^+ and D^+($^2H^+$) on Ru specimen exposed to $2.5x10^{-7}$ mbar of N_2+H_2 gas mixture at 300 K overlayed with the corresponding FIM image.

While it may be disappointing not to observe any recombination between N and ²H atoms on the surface, it is important to note that this is the most expected result. Beyond the extremely low temperature for a potential Haber-Bosch reaction, the electric field is applied in the form of high-frequency electric pulses (between 25 and 200 kHz), which may prevent any possible reaction between N and H, as was the case for O_2 + H_2 on Fe. Nevertheless, the ability to dissociate N_2 so easily at room temperature opens new avenues for investigation. Other electric field applications must be explored to give N and H a chance to recombine and react, while maintaining the ability to probe and measure the surface composition as the reaction occurs.

3.3 Surface electric field and impact on N_2 Molecular orbitals

The development of OAP must be accompanied by a better understanding of the impacts of electric fields (EF) on reactivity. Shawn Kathmann (PNNL) is applying quantum mechanical calculations to model the deformation of N_2's HOMO and LUMO as the molecule evolves in a space with a strong electric field (1, 5, and 10 V/Å). On **Figure 3.10**.A, we can see that HOMO deformation is observed starting at 10 V/nm (1.0 V/Å). As the field strength increases toward 100 V/nm, the HOMO is fully polarized along the EF axis. A similar behavior is observed with the LUMO, where polarization begins at 10 V/nm, but the LUMO completely changes at 50 V/nm. The intense EF does not deform all orbitals equally and can stabilize higher LUMO+n states, altering the sequence of energy levels in the molecular orbitals. The calculation of the iso-electrical potential surrounding the N_2 molecule also provides a clear visualization of the effect of an intense EF perpendicular to the N-N axis, with the N_2 electron cloud fully polarized by the EF vector.

As calculated by Kreuzer et al.[21], the presence of an electric field significantly alters the molecular orbitals and electronic distribution of N_2, changing its chemical properties and reactivity. This effect likely explains why we observed the dissociative adsorption of N_2 on Ru, even at relatively low temperatures. However, we must acknowledge that the electric field required to observe such deformation is extremely intense. According to Kingham's predictions and field evaporation estimates, only pure carbon specimens may withstand such intense electric fields without field evaporation. It is also important to consider that the EF on matter is inhomogeneous.

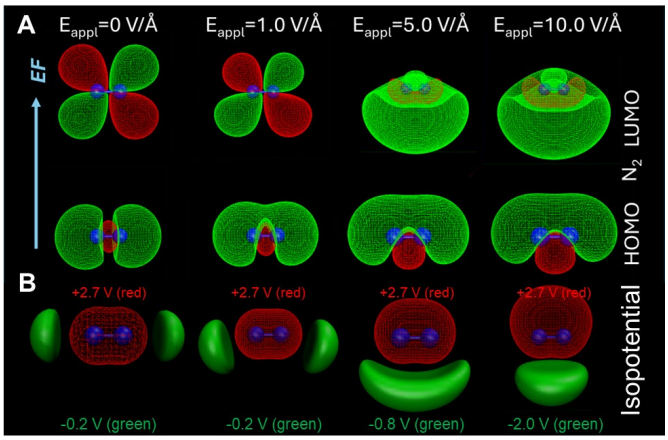

Figure 3. 10: (A) QM calculation of N_2 HOMO and LUMO deformation once the N_2 present in an EF perpendicular to the N-N axis. (B) Iso-electrical-potential surrounding the N_2 molecule while applying different intensity of EF (0, 1, 5 and 10 V/Å)

Electric fields are generated when there is an uneven distribution of electric charges in space. Since atoms and molecules consist of positively charged nuclei surrounded by negatively charged

electron clouds, an electric field exists near all matter, even if the matter is neutral overall. As one approaches the surface of matter, the electric field strength increases, reaching values as high as 100 V/nm, as shown on the left side of **Figure 3.11**. Similar to Earth's gravitational field, the force vectors of the electric field converge toward each nucleus. This convergence creates a gradient, with the electric field becoming more intense closer to the surface.

As it can deform N_2 molecular orbitals, the application of an external electric field will also deform the gradient of electric fields present at the surface of a Ru cluster, as depicted on the right side of **Figure 3.11.** One can observe that the modest application of a 10 V/nm external field can drastically expand the region around the cluster where the electric field exceeds 10 V/nm, providing more opportunities for an approaching molecule like N_2 to be polarized and electronically activated by the field. The electric field not only changes the chemical properties of nearby molecules but also alters the chemical properties of the electrified surface itself.

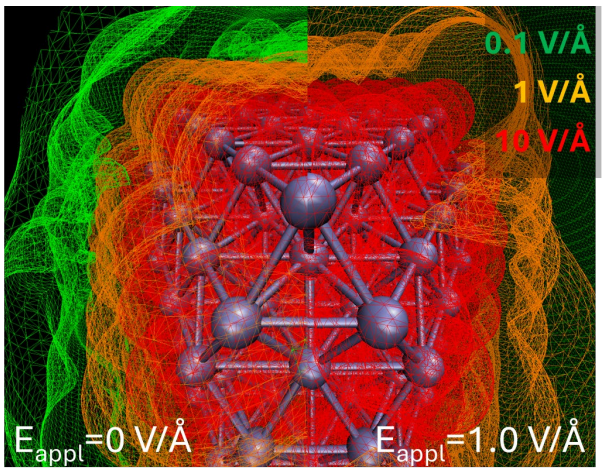

Figure 3.11: Iso-electrical field of 0.1, 1 and 10 V/Å surrounding a Ru cluster with/without applying an external electric field of 1.0 V/Å.

3.4 Conclusions and perspectives

Combined with FIM, the OAP approach has successfully detected the dissociative adsorption of N_2 and H_2 at room temperature. We have observed that Ru(0001), {10-12}, and {11-24} play important roles in these dissociations. While accurately estimating the electric field values at the surface remains challenging, FIM surface characterization, supported by a better understanding of the effect of electric fields through quantum mechanics calculations, has helped us refine these estimations. Using Kingham plots, we were able to narrow down the electric field intensity of interest to between 13 and 15 V/nm. Shawn Kathmann is currently deepening his investigation of this system with the aim of a joint publication, which will solidify OAP as a technique of choice for studying field-assisted chemistry and open new research opportunities as we continue to develop the instrument based on technical advancements and research needs.

In terms of experimentation, considering the need for intense electric fields to observe extreme surface phenomena, we are currently preparing C(diamond) specimens in collaboration with Prof. Peter Pauzauskie (University of Washington) with the objective of applying extreme electric fields to their surfaces and attempting to observe N_2 dissociation on C(diamond).

4.0 Technical developments of OAP

The development of a new atom probe has been more complex than expected, particularly in terms of cost and the feasibility of including a Raman detector in the chamber. The APT specimen is extremely fragile and small, and the Raman spectroscopy setup would require positioning the Raman optics less than 1 mm away from the specimen's apex, which proved too challenging for the scope of this project. We conclude that it would be more effective to use the pre-existing LEAP4000 setup in collaboration with the vendor. Despite the absence of Raman, we have improved our electric field estimation through a more detailed interpretation of our FIM images and by developing a method using Kingham plots and APT mass spectra at different temperatures. After adapting our OAP setup for investigations involving hydrogen on the more modern LEAP5000, by installing a line of $^{2}H_2$ and a line of $^{18}O_2$, we continued to develop the OAP by enhancing the data analysis and high-temperature capabilities.

4.1 OAP results analytic software

In collaboration with intern Eric Vo, we developed an algorithm that directly reads APT data and converts it into OAP data. Previously, OAP data were created using the vendor's data analysis software, "IVAS," which does not record the experimental time. The LEAP4000 records ions as a series of events. Each event is identified by its time of flight, the x and y positions where the event was detected on the detector, and an electric pulse number. Practically, if an electric pulse does not trigger a signal on the detector, nothing is recorded. However, if a signal is detected, it is recorded as an event. The issue was that the number of pulses is recorded on a 24-bit memory, which limits the count to a maximum of 16,777,215 pulses before the memory resets to 0.

The first process in the OAP software was to correct for these resets and re-estimate the experiment's timeline. This process creates a cloud of events over time. The events are then translated into ions, which are eventually identified using the .RRNG file created by the user.

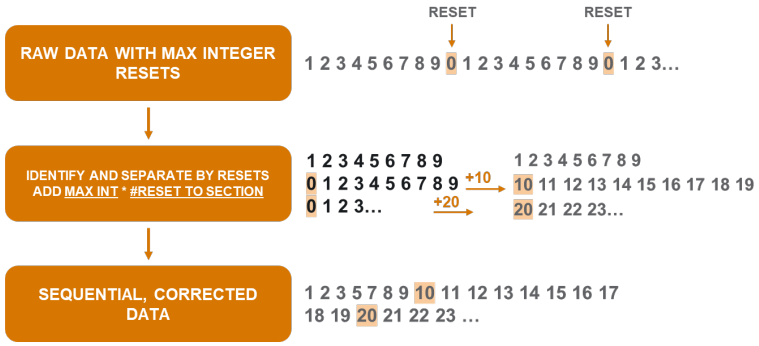

The second part of the software allows to create heat maps automatically from this cloud of events and measure the local concentration over the time. The next step of the development of this software is to improve its autonomy form IVAS, improve the Graphical User Interface and add an automatic peak identification on the long term. This software is already used to support AI-assisted OAP development.

4.2 High temperature specimen holder

One of the major limitations of modern APT is the inability to increase the specimen's temperature above 320 K. Modern APT machines are complex with delicate parts that may be sensitive to high temperatures. Our proposal was to develop a sample holder that heats only a very small part

of the assembly, specifically the specimen itself, while keeping the rest at cryogenic temperatures. Inspired by previous designs, which were in turn inspired by light bulbs, we developed our own version. The specimen is mounted facing a counter electrode, welded to a Ni contact that is connected to a W bridge.

The sample holder consists of a polyimide upper plate, known for its heat resistance and electrical insulation, and a MACOR bottom plate, which is also electrically insulating but a good thermal conductor to transfer cold from the sample stage. While the heating of the tungsten bridge has been successfully tested (the W bridge reaches temperatures higher than 1000°C), the heat transfer to the needle is still in the testing phase, which is expected to be completed in October 2024.

If you want I can shhow you quickly how It rfwewefsefsdfsdf

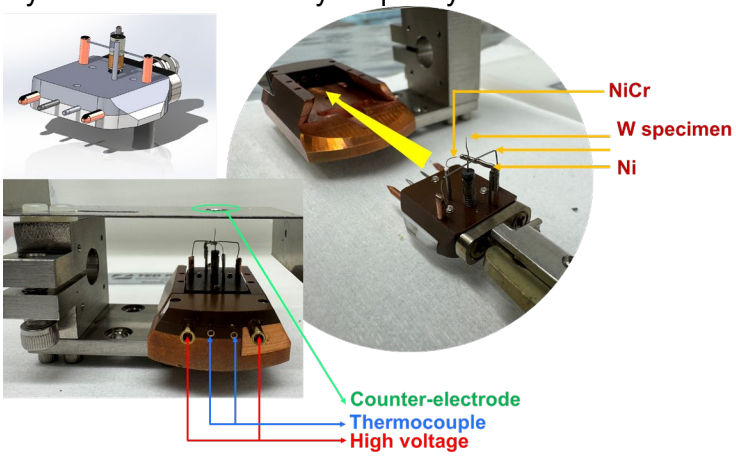

5.0 References

1. Mcewen, J. *et al.* Catalytic Reduction of NO 2 with Hydrogen on Pt Field Emitter Tips : Kinetic Instabilities on the Nanoscale †. **26**, 16381–16391 (2010).

2. van Tol, M. F. H., Gielbert, A., Wolf, R. M., Lie, A. B. K. & Nieuwenhuys, B. E. The striking difference in the behaviour of Rh and Pt towards their interaction with CO_2. *Surf. Sci.* **287–288**, 201–207 (1993).

3. van Tol, M. F. H., Gielbert, A. & Nieuwenhuys, B. E. The adsorption and dissociation of CO_2 on Rh. *Appl. Surf. Sci.* **67**, 166–178 (1993).

4. Cranstoun, G. K. L. & Lynch, J. T. Field ion microscope studies of the oxidation of iron. *Appl. Surf. Sci.* **5**, 161–179 (1980).

5. McEwen, J. S., Gaspard, P., Visart De Bocarmé, T. & Kruse, N. Oscillations and bistability in the catalytic formation of water on rhodium in high electric fields. *J. Phys. Chem. C* **113**, 17045–17058 (2009).

6. Owczarek, S. *et al.* Oxygen Adsorption, Subsurface Oxygen Layer Formation and Reaction with Hydrogen on Surfaces of a Pt–Rh Alloy Nanocrystal. *Top. Catal.* **63**, 1522–1531 (2020).

7. Lambeets, S. V. *et al.* Adsorption and hydrogenation of CO_2 on Rh nanosized crystals demonstration of the role of inter-facet oxygen spillover and comparative studies with O_2, N_2O and CO. *J. Phys. Chem. C* **121**, 16238–16429 (2017).

8. McEwen, J. S., Gaspard, P., Mittendorfer, F., de Bocarmé, T. V. & Kruse, N. Field-assisted oxidation of rhodium. *Chem. Phys. Lett.* **452**, 133–138 (2008).

9. Barroo, C., De Decker, Y., Jacobs, L. & de Bocarmé, T. V. Nonlinear behavior during NO2 hydrogenation on a nanosized Pt-Rh catalyst sample. *Appl. Surf. Sci.* **412**, 564–570 (2017).

10. Lambeets, S. V. *et al.* Nanoscale Perspectives of Metal Degradation via In Situ Atom Probe Tomography. *Top. Catal.* **63**, 1606–1622 (2020).

11. Janssen, N. M. H., van Tol, M. F. H. & Nieuwenhuys, B. E. The interaction of oxygen with Rh studied by field electron microscopy. *Appl. Surf. Sci. 74* **74**, 1–12 (1994).

12. Gorodetskii, V. V., Elokhin, V. I., Bakker, J. W. & Nieuwenhuys, B. E. Field electron and field ion microscopy studies of chemical wave propagation in oscillatory reactions on platinum group metals. *Catal. Today* **105**, 183–205 (2005).

13. Rezeq, M., Pitters, J. & Wolkow, R. Tungsten nanotip fabrication by spatially controlled field-assisted reaction with nitrogen. *J. Chem. Phys.* **124**, 2047`1 (2006).

14. Hong, Y., Hensley, A., McEwen, J. S. & Wang, Y. Perspective on Catalytic Hydrodeoxygenation of Biomass Pyrolysis Oils: Essential Roles of Fe-Based Catalysts.

Catal. Letters **146**, 1621–1633 (2016).

15. Rogers, K. A. & Zheng, Y. Selective Deoxygenation of Biomass-Derived Bio-oils within Hydrogen-Modest Environments: A Review and New Insights. *ChemSusChem* **9**, 1750–1772 (2016).

16. Bray, J. *et al.* Modeling the adsorbate coverage distribution over a multi-faceted catalytic grain in the presence of an electric field: O/Fe from first principles. *Catal. Today* **312**, 92–104 (2018).

17. Wen, X. & Guan, J. Recent advancement in the electrocatalytic synthesis of ammonia. *Nanoscale* **12**, 8065–8094 (2020).

18. Wan, M., Yue, H., Notarangelo, J., Liu, H. & Che, F. Deep Learning-Assisted Investigation of Electric Field–Dipole Effects on Catalytic Ammonia Synthesis. *JACS Au* **2**, 1338–1349 (2022).

19. Che, F. *et al.* Elucidating the Roles of Electric Fields in Catalysis: A Perspective. *ACS Catal.* **8**, 5153–5174 (2018).

20. Che, F., Gray, J. T., Ha, S. & McEwen, J.-S. Reducing Reaction Temperature, Steam Requirements, and Coke Formation During Methane Steam Reforming Using Electric Fields: A Microkinetic Modeling and Experimental Study. *ACS Catal.* **7**, 6957–6968 (2017).

21. Karahka, M. L. & Kreuzer, H. J. New physics and chemistry in high electrostatic fields. *Surf. Sci.* **643**, 164–171 (2016).

22. Kreuzer, H. J. Field-Induced Chemistry in Catalysis: High Pressure and High Fields. *Top. Catal.* **63**, 1497–1501 (2020).

23. Kathmann, S. M. Electric fields and potentials in condensed phases. *Phys. Chem. Chem. Phys.* **23**, 23836–23849 (2021).

24. Oppenheimer, J. R. Three Notes on the quantum theroy of aperiodic effects. *Phys. Rev.* **13**, 66–81 (1928).

25. Müller, E. & Tsong, T. T. *Field Ion Microscopy Principles and Applications*. (Elsevier Publishing Company, Inc., 1969).

26. Gault, B., Moody, M. P., Cairney, J. M. & Ringer, S. P. *Atom Probe Microscopy*. (2012). doi:10.1007/978-1-4614-3436-8.

27. Miller, M. K., Cerezo, A., Hetherington, M. G. & Smith, G. D. W. *Atom Probe Field Ion Microscopy*. (Claredon Press, 1996).

28. Tsong, T. T. Field Ion Image Formation. *Surf. Sci.* **70**, 211–233 (1978).

29. Kingham, D. R. The post-ionization of field evaporated ions: A theoretical explanation of

multiple charge states. *Surf. Sci.* **116**, 273–301 (1982).

30. Levi Tegg, Leigh T Stephenson, J. M. C. Estimation of the electric field in atom probe tomography experiments using charge state ratios. *Microsc. Microanal.* **30**, 466–475 (2024).

31. Von der Lage, F. C. & Bethe, H. A. A Method for Obtaining Electronic Eigenfunctions and Eigenvalues in Solids with An Application to Sodium. *Phys. Rev.* **71**, 612–622 (1947).

32. McCarroll, I. E. *et al.* The effect of hydrogen on the early stages of oxidation of a magnesium alloy. *Corros. Sci.* **165**, 108391 (2020).

33. Cranstoun, G. K. L. & Anderson, J. Hydrogen promoted corrosion of tungsten by oxygen in an electric field: a field ion microscope study. *Surf. Sci.* **35**, 319–335 (1973).

34. Nowak, C., Schmitz, G. & Kirchheim, R. Electric field effect on low temperature nanoscale oxidation. *Surf. Sci.* **604**, 641–648 (2010).

35. Karahka, M., Xia, Y. & Kreuzer, H. J. The mystery of missing species in atom probe tomography of composite materials. *Appl. Phys. Lett.* **107**, 2–6 (2015).

36. Müller, E. W., Nakamura, S., Nishikawa, O. & McLane, S. B. Gas-surface interactions and field-ion microscopy of nonrefractory metals. *J. Appl. Phys.* **36**, 2496–2503 (1965).

37. Yüzbasioglu, A. E., Avsar, C. & Gezerman, A. O. The current situation in the use of ammonia as a sustainable energy source and its industrial potential. *Curr. Res. GReen Sustain. Chemsitry* **5**, 100307 (2022).

38. Rizzato, L., Cavazzani, J., Glisenti, A. & Osti, A. N_2 solar activation : ammonia as a hydrogen vector for energy storage. *Faraday Discuss.* **243**, 388–401 (2023).

39. Tawalbeh, M. *et al.* Ammonia : A versatile candidate for the use in energy storage systems. *Renew. Energy* **194**, 955–977 (2022).

40. Aresta, M., Dibenedetto, A. & Quaranta, E. *Reaction Mechanisms in Carbon Dioxide Conversion*. (Springer, 2016). doi:10.1007/978-3-662-46831-9.

41. Yousaf, M. *et al.* Carbon dioxide utilization : A critical review from multiscale perspective. 4890–4923 (2022) doi:10.1002/ese3.1303.

42. Mulson, J. F. & Müller, E. W. Corrosion of Tungsten and Iridium by Field Desorption of Nitrogen and Carbon Monoxide □. *J. Chem. Phys.* **38**, 2615–2619 (1963).

43. Logadóttir, Á. & Nørskov, J. K. Ammonia synthesis over a Ru (0001) surface studied by density functional calculations. **220**, 273–279 (2003).

44. Wang, Y. & Guo, H. Post-dissociation Dynamics of N 2 on Ru (0001): How Far Can the " Hot " N Atoms Travel ? (2023) doi:10.1021/acs.jpcc.2c08671.

45. Wagner, J., Grabnic, T. & Sibener, S. J. STM Visualization of N 2 Dissociative Chemisorption on Ru(0001) at High Impinging Kinetic Energies. (2022) doi:10.1021/acs.jpcc.2c05770.

Appendix A – List of APT experiment with ID # runs

LDRD APT experiment list

Run#	Specimen ID	Surf Composition	APT	Inst.	Gas used	Type of Exp.
18114	Fe$016	Fe	LEAP4000	APT	none	Surface cleaning
18115	Fe$016	Fe	LEAP4000	FIM	Ne	Surface characterization
18116	Fe$016	Fe	LEAP4000	OAP	none	EF measure
18117	Fe$016	Fe	LEAP4000	APT	none	cleaning
18119	Fe$016	Fe	LEAP4000	OAP	N2	N2 dissociation
18120	Fe$016	Fe	LEAP4000	OAP	O2	Fe oxidation
18121	Fe$016	Fe	LEAP4000	OAP	O2	Fe oxidation
18122	Fe$016	Fe	LEAP4000	OAP	O2	Fe oxidation
18123	Fe$016	Fe	LEAP4000	APT	none	cleaning
18124	Fe$016	Fe	LEAP4000	OAP	O2	Fe oxidation
18125	Fe$016	Fe	LEAP4000	APT	none	cleaning
18126	Fe$016	Fe	LEAP4000	OAP	O2	Fe oxidation
18144	Fe$016	Fe	LEAP4000	APT	none	EF measure
18148	Fe$016	Fe	LEAP4000	APT	none	EF measure
19270	Fe$020	Fe	LEAP4000	APT	none	Surface cleaning
19271	Fe$023	Fe	LEAP4000	APT	none	Surface cleaning
19272	Fe$023	Fe	LEAP4000	FIM	Ne	Surface characterization
19273	Fe$022	Fe	LEAP4000	APT	none	Surface cleaning
19274	Fe$022	Fe	LEAP4000	FIM	Ne	Surface characterization
19275	Fe$021	Fe	LEAP4000	APT	none	Surface cleaning
19276	Fe$021	Fe	LEAP4000	FIM	Ne	Surface characterization
20569	MGW_V2_21_M2	Ru	LEAP4000	APT	none	APT analysis
20570	MGW_V2_21_M4	Ru	LEAP4000	APT	none	APT analysis
20571	MGW_V2_21_M4	Ru	LEAP4000	FIM	Ne	Surface characterization
20572	MGW_V2_21_M4	Ru	LEAP4000	APT	none	APT analysis
20574	MGW_V2_21_M4	Ru	LEAP4000	FIM	Ne	Surface characterization
20576	MGW_V2_21_M4	Ru	LEAP4000	OAP	N2	N2 dissociation
20577	MGW_V2_21_M4	Ru	LEAP4000	APT	none	APT analysis
20578	MGW_V2_21_M4	Ru	LEAP4000	APT	none	APT analysis
20580	MGW_V2_21_M7	Ru	LEAP4000	APT	none	APT analysis
20581	MGW_V2_21_M7	Ru	LEAP4000	FIM	Ne	Surface characterization
20755	MGW_V2_21_M7	Ru	LEAP4000	APT	none	EF measure

20756	MGW_V2_21_M7	Ru	LEAP4000	FIM	Ne	Surface characterization
20758	MGW_V2_21_M7	Ru	LEAP4000	OAP	N2	N2 dissociation
20759	MGW_V2_21_M7	Ru	LEAP4000	APT	none	EF measure
20760	MGW_V2_21_M7	Ru	LEAP4000	APT	none	EF measure
20783	MGW_V2_21_M3	Ru	LEAP4000	APT	none	Surface cleaning
20784	MGW_V2_21_M3	Ru	LEAP4000	FIM	Ne	Surface characterization
20786	MGW_V2_21_M5	Ru	LEAP4000	APT	none	Surface cleaning
20787	MGW_V2_21_M5	Ru	LEAP4000	FIM	Ne	Surface characterization
20789	MGW_V2_21_M5	Ru	LEAP4000	FIM	Ne	Surface characterization
20789	MGW_V2_21_M5	Ru	LEAP4000	APT	none	EF measure
20801	MGW_V2_21_M5	Ru	LEAP4000	OAP	N2	N2 dissociation
20804	MGW_V2_21_M5	Ru	LEAP4000	APT	none	Surface cleaning
20805	MGW_V2_21_M5	Ru	LEAP4000	OAP	N2	N2 dissociation
20806	MGW_V2_21_M5	Ru	LEAP4000	APT	none	Surface cleaning
20807	MGW_V2_21_M5	Ru	LEAP4000	APT	none	EF measure
20808	MGW_V2_21_M5	Ru	LEAP4000	OAP	N2	N2 dissociation
20809	MGW_V2_21_M5	Ru	LEAP4000	APT	none	Surface cleaning
21150	SVL_V3_04_M1	Ru	LEAP4000	APT	none	Surface cleaning
21152	SVL_V3_04_M1	Ru	LEAP4000	FIM	Ne	Surface characterization
21153	SVL_V3_04_M3	Ru	LEAP4000	APT	none	Surface cleaning
21158	SVL_V3_04_M2	Ru	LEAP4000	APT	none	Surface cleaning
21159	SVL_V3_04_M2	Ru	LEAP4000	FIM	Ne	Surface characterization
21160	SVL_V3_04_M4	Ru	LEAP4000	APT	none	Surface cleaning
21161	SVL_V3_04_M4	Ru	LEAP4000	FIM	Ne	Surface characterization
21163	SVL_V3_04_M6	Ru	LEAP4000	APT	none	Surface cleaning
21164	SVL_V3_04_M6	Ru	LEAP4000	APT	none	Surface cleaning
21165	SVL_V3_04_M8	Ru	LEAP4000	APT	none	Surface cleaning
21166	SVL_V3_04_M8	Ru	LEAP4000	FIM	Ne	Surface characterization
21167	SVL_V3_04_M10	Ru	LEAP4000	APT	none	Surface cleaning
21168	Fe$023	Fe	LEAP4000	APT	none	Surface cleaning
21169	Fe$023	Fe	LEAP4000	FIM	Ne	Surface characterization
21170	Fe$022	Fe	LEAP4000	APT	none	Surface cleaning
21171	Fe$022	Fe	LEAP4000	FIM	Ne	Surface characterization
21173	Fe$021	Fe	LEAP4000	APT	none	Surface cleaning
21175	Fe$024	Fe	LEAP4000	APT	none	Surface cleaning
21177	Fe$027	Fe	LEAP4000	APT	none	Surface cleaning

21178	Fe$026	Fe	LEAP4000	APT	none	Surface cleaning
21179	Fe$026	Fe	LEAP4000	FIM	Ne	Surface characterization
21181	Fe$025	Fe	LEAP4000	APT	none	Surface cleaning
21182	Fe$025	Fe	LEAP4000	FIM	Ne	Surface characterization
21200	Fe$024	Fe	LEAP4000	APT	none	Surface cleaning
21201	Fe$025	Fe	LEAP4000	APT	none	Surface cleaning
21203	Fe$026	Fe	LEAP4000	APT	none	Surface cleaning
21204	Fe$026	Fe	LEAP4000	APT	none	Surface cleaning
21206	Fe$026	Fe	LEAP4000	OAP	N2	N2 dissociation
21208	Fe$026	Fe	LEAP4000	OAP	N2	N2 dissociation
21209	Fe$026	Fe	LEAP4000	OAP	N2	N2 dissociation
21210	Fe$026	Fe	LEAP4000	OAP	N2	N2 dissociation
21211	Fe$026	Fe	LEAP4000	OAP	N2	N2 dissociation
21215	Fe$026	Fe	LEAP4000	OAP	N2	N2 dissociation
21216	Fe$026	Fe	LEAP4000	OAP	N2	N2 dissociation
21217	Fe$026	Fe	LEAP4000	OAP	N2	N2 dissociation
21219	Fe$026	Fe	LEAP4000	OAP	N2	N2 dissociation
21220	Fe$026	Fe	LEAP4000	OAP	N2	N2 dissociation
21221	Fe$026	Fe	LEAP4000	OAP	N2	N2 dissociation
21222	Fe$026	Fe	LEAP4000	OAP	N2	N2 dissociation
21223	Fe$026	Fe	LEAP4000	OAP	N2	N2 dissociation
21224	Fe$026	Fe	LEAP4000	OAP	N2	N2 dissociation
21225	Fe$026	Fe	LEAP4000	OAP	N2	N2 dissociation
21226	Fe$026	Fe	LEAP4000	OAP	N2	N2 dissociation
21227	Fe$026	Fe	LEAP4000	OAP	N2	N2 dissociation
21228	Fe$026	Fe	LEAP4000	OAP	N2	N2 dissociation
21229	Fe$026	Fe	LEAP4000	OAP	N2	N2 dissociation
21230	Fe$026	Fe	LEAP4000	OAP	N2	N2 dissociation
21263	SVL_V3_04_M4	Ru	LEAP4000	APT	none	Surface cleaning
21264	SVL_V3_04_M4	Ru	LEAP4000	OAP	N2	N2 dissociation
21267	SVL_V3_04_M4	Ru	LEAP4000	APT	none	Surface cleaning
21268	SVL_V3_04_M4	Ru	LEAP4000	OAP	none	EF measure
21269	SVL_V3_04_M4	Ru	LEAP4000	OAP	N2	N2 dissociation
21270	SVL_V3_04_M4	Ru	LEAP4000	OAP	none	EF measure
21271	SVL_V3_04_M4	Ru	LEAP4000	OAP	N2	N2 dissociation
21272	SVL_V3_04_M4	Ru	LEAP4000	OAP	none	EF measure

21273	SVL_V3_04_M4	Ru	LEAP4000	OAP	N2	N2 dissociation
21274	SVL_V3_04_M4	Ru	LEAP4000	OAP	none	EF measure
21275	SVL_V3_04_M4	Ru	LEAP4000	OAP	N2	N2 dissociation
21276	SVL_V3_04_M4	Ru	LEAP4000	OAP	none	EF measure
21277	SVL_V3_04_M4	Ru	LEAP4000	OAP	none	EF measure
21278	SVL_V3_04_M4	Ru	LEAP4000	OAP	none	EF measure
21279	SVL_V3_04_M4	Ru	LEAP4000	OAP	N2	N2 dissociation
21280	SVL_V3_04_M4	Ru	LEAP4000	OAP	none	EF measure
31279	SVL_V3_04_M4	Ru	LEAP4000	OAP	N2	N2 dissociation
31447	Fe$026	Fe	LEAP4000	OAP	CH4	CH4 dissociation
31448	Fe$026	Fe	LEAP4000	OAP	CH4	CH4 dissociation
31449	Fe$026	Fe	LEAP4000	OAP	CH4	CH4 dissociation
31647	Fe$026	Fe	LEAP4000	OAP	O2	Fe oxidation
31648	Fe$026	Fe	LEAP4000	OAP	O2	Fe oxidation
33386	Fe$030	Fe	LEAP5000	APT	none	Surface cleaning
33387	Fe$030	Fe	LEAP5000	FIM	Ne	Surface characterization
33388	Fe$029	Fe	LEAP5000	APT	none	Surface cleaning
33389	Fe$029	Fe	LEAP5000	FIM	Ne	Surface characterization
33419	Fe$030	Fe	LEAP5000	APT	none	Surface cleaning
33420	Fe$030	Fe	LEAP5000	FIM	Ne	Surface characterization
33421	Fe$029	Fe	LEAP5000	APT	none	Surface cleaning
33422	Fe$029	Fe	LEAP5000	FIM	Ne	Surface characterization
33423	Fe$028	Fe	LEAP5000	APT	none	Surface cleaning
33424	Fe$028	Fe	LEAP5000	FIM	Ne	Surface characterization
33440	SVL_05272024_Ru_M1	Ru	LEAP5000	APT	none	Surface cleaning
33441	SVL_05272024_Ru_M1	Ru	LEAP5000	FIM	Ne	Surface characterization
33443	SVL_05272024_Ru_M3	Ru	LEAP5000	APT	none	Surface cleaning
33444	SVL_05272024_Ru_M3	Ru	LEAP5000	FIM	Ne	Surface characterization
33445	SVL_05272024_Ru_M5	Ru	LEAP5000	APT	none	Surface cleaning
33446	SVL_05272024_Ru_M5	Ru	LEAP5000	FIM	Ne	Surface characterization
33447	SVL_05272024_Ru_M7	Ru	LEAP5000	APT	none	Surface cleaning
33448	SVL_05272024_Ru_M7	Ru	LEAP5000	FIM	Ne	Surface characterization
33450	SVL_05272024_Ru_M4	Ru	LEAP5000	APT	none	Surface cleaning
33451	SVL_05272024_Ru_M4	Ru	LEAP5000	FIM	Ne	Surface characterization
33452	SVL_05272024_Ru_M6	Ru	LEAP5000	APT	none	Surface cleaning
33453	SVL_05272024_Ru_M6	Ru	LEAP5000	FIM	Ne	Surface characterization

33488	SVL_05272024_Ru_M1	Ru	LEAP5000	OAP	N2+D2	N2 hydrogenation
33490	SVL_05272024_Ru_M3	Ru	LEAP5000	OAP	N2	N2 dissociation
33492	SVL_05272024_Ru_M5	Ru	LEAP5000	OAP	N2	N2 dissociation
33495	SVL_05272024_Ru_M5	Ru	LEAP5000	OAP	N2+D2	N2 hydrogenation
33496	SVL_05272024_Ru_M5	Ru	LEAP5000	OAP	N2+D2	N2 hydrogenation
33498	SVL_05272024_Ru_M5	Ru	LEAP5000	OAP	N2	N2 dissociation
33499	SVL_05272024_Ru_M7	Ru	LEAP5000	OAP	N2	N2 dissociation
33500	Fe$029	Fe	LEAP5000	APT	none	Surface cleaning
33502	Fe$029	Fe	LEAP5000	OAP	O2+H2	O2 hydrogenation
10967	Fe$029	Fe	LEAP5000	APT	none	Surface cleaning
10968	Fe$029	Fe	LEAP5000	APT	none	Surface cleaning
10969	Fe$029	Fe	LEAP5000	OAP	O2+H2	O2 hydrogenation

Pacific Northwest National Laboratory

902 Battelle Boulevard
P.O. Box 999
Richland, WA 99354

1-888-375-PNNL (7665)

www.pnnl.gov